



Review

Silver-based semiconductor Z-scheme photocatalytic systems for environmental purification



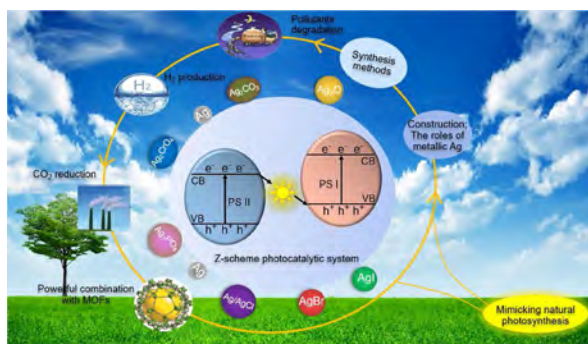
Wenjing Xue^{a,b}, Danlian Huang^{a,b,*}, Xiaojun Wen^c, Sha Chen^{a,b}, Min Cheng^{a,b}, Rui Deng^{a,b}, Bo Li^{a,b}, Yang Yang^{a,b}, Xigui Liu^{a,b}

^a College of Environmental Science and Engineering, Hunan University, Changsha, 410082, PR China

^b Key Laboratory of Environmental Biology and Pollution Control (Hunan University), Ministry of Education, Hunan University, Changsha, 410082, PR China

^c School of Chemistry and Environmental Engineering, Yancheng Teachers University, Xiwang Road, Yancheng, Jiangsu Province, 224051, PR China

GRAPHICAL ABSTRACT



ARTICLE INFO

Editor: Danmeng Shuai

Keywords:

Silver-based semiconductor
Organic pollutants degradation
Photocatalytic hydrogen production
Carbon dioxide reduction
Metal organic frameworks

ABSTRACT

Silver-based semiconductor photocatalysts are promising materials for solving environmental and energy issues due to their strong optical absorption, excellent quantum efficiency and photoelectrochemical properties. However, the uncontrollable photocorrosion and high use cost of single silver-based semiconductor photocatalysts limit its practical application. The construction of Z-scheme photocatalytic systems that mimic natural photosynthesis can not only enhance the photocatalytic activity of silver-based semiconductor photocatalysts, but also improve their stability and reduce the use costs. This critical review concisely highlights the basic principles of Z-scheme photocatalytic systems, and discusses the construction of silver-based semiconductor Z-scheme photocatalytic systems and the roles of metallic Ag in there and summarizes the synthesis methods of silver-based semiconductor Z-scheme photocatalytic systems. Then, a series of the solar-driven applications are elaborated, including organic pollutants degradation, hydrogen production, and carbon dioxide reduction. Meanwhile, the mechanism and difficult level of these photocatalytic reactions are also described. Besides, metal organic frameworks (MOFs) as a novel type of photocatalysts have attracted growing attention. The novel combination of silver-based semiconductor with typical photoactive MOFs is highlighted based on the Z-scheme photocatalytic systems. Eventually, the future challenges and prospects in the development of silver-based semiconductor Z-scheme photocatalytic systems are presented.

* Corresponding author at: College of Environmental Science and Engineering, Hunan University, Changsha, 410082, PR China.

E-mail address: huangdanlian@hnu.edu.cn (D. Huang).

<https://doi.org/10.1016/j.jhazmat.2020.122128>

Received 9 October 2019; Received in revised form 28 December 2019; Accepted 16 January 2020

Available online 26 January 2020

0304-3894/ © 2020 Elsevier B.V. All rights reserved.

1. Introduction

Nowadays, environmental and energy issues are the focus of global concern (Xiao et al., 2017; Wen et al., 2018a; Yang et al., 2019a; Guo et al., 2018a; Huang et al., 2017a). To solve these problems, especially the consumption of fossil fuels and their harms to environment, tremendous efforts have been made toward exploring clean and new renewable energy resource. Semiconductor photocatalysis has attracted considerable attention for its promising potential to address intractable environmental and energy issues using abundant solar energy (Yang et al., 2019b; Wang et al., 2019; Liu et al., 2018a). Particularly, it has exhibited the huge potential in organic pollutants degradation (Xiao et al., 2017; Wen et al., 2017; Huang et al., 2013; Li et al., 2019a; Shao et al., 2018b, 2017), water splitting to produce hydrogen (H_2) and/or oxygen (O_2) (Liu et al., 2016; Ye et al., 2016), and carbon dioxide (CO_2) reduction to generate renewable fuels (Sorcar et al., 2017; Li et al., 2015a; Huang et al., 2019a). The most widely investigated traditional semiconductor photocatalyst is TiO_2 owing to its structural stability and low cost (Yu et al., 2013; Xue et al., 2018a). However, TiO_2 can only utilize ultraviolet light which accounts for 4 % of sunlight owing to its large band gap. Therefore, developing new and efficient visible light photocatalyst has become the hotspot research in the photocatalytic field.

Among various visible-light-driven photocatalysts, silver-based semiconductors are photosensitive materials that have been widely used in photographic films for more than 200 years, which exhibits the outstanding photoresponse property (Xu et al., 2015a; Chen et al., 2019). For example, Ag_3PO_4 could obtain a significantly high quantum yield of 90 % for water oxidation under visible light irradiation (Yi et al., 2010). Wang et al. Wang et al. (2008) reported a plasmonic photocatalyst $Ag@AgCl$ possessed highly efficient photocatalytic activity for organic pollutants degradation under visible light. Compared with most semiconductor materials, the conduction band (CB) potential of AgI is more negative, and when it is loaded on other catalyst surfaces, it can effectively promote the separation of carriers. Besides, some silver-based semiconductors present excellent visible light photocatalytic activities towards H_2 production and CO_2 reduction (An et al., 2012, 2013). The outstanding performance of silver-based semiconductor materials should be attributed to the distinctive filled d^{10} electronic configuration of Ag^+ ions which involves the formation and the hybridization of the energy band structure (Dong et al., 2014). Thus, due to their many advantages, such as strong optical absorption ability, excellent quantum efficiency and photocatalytic activity, silver-based semiconductor photocatalysts have aroused great concern and interest. Generally, the photocatalytic reaction mainly includes four processes: (1) generating photogenerated electron-hole pairs by absorbing sunlight, (2) the separation and transfer of photogenerated carriers, (3) participating the oxidation/reduction reaction on the surface of photocatalyst, and (4) photogenerated carriers' recombination in bulk or on the surface of photocatalyst (Bai et al., 2015). The thermodynamics and kinetics of the processes above determined the efficiency of photocatalyst. However, for single-component silver-based semiconductor photocatalyst, the limited visible-light absorption and low oxidation/reduction ability restrain its wider application. And the photogenerated electrons and holes in single component photocatalysts easily recombine owing to the strong Coulombic force between electrons and holes (Fig. 1a) (Low et al., 2017; Huang et al., 2017b). Moreover, poor stability, high cost and easy aggregation also limit the practical applications of single-component silver-based semiconductor photocatalysts.

Fortunately, studies have confirmed that the construction of heterostructure photocatalytic system (usually type-II systems (Fig. 1b)) that comprises two semiconductors with suitable bandgap, is an effective strategy to improve photocatalytic efficiency because of their advantages in separating photogenerated carriers and increasing light-absorption range. For example, Zhou et al. Zhou et al. (2018a)

constructed a type-II $AgI/Bi_{12}O_{17}Cl_2$ heterojunction photocatalyst through a deposition-precipitation method. The AgI (25 wt. %)/ $Bi_{12}O_{17}Cl_2$ exhibited the optimal photocatalytic activity for sulfamethazine degradation under visible light, approximately 7.0 and 7.8 times higher than that of single AgI and $Bi_{12}O_{17}Cl_2$. The introduction of $Bi_{12}O_{17}Cl_2$ not only enhanced the photostability of AgI, but also reduced the amount and cost of AgI. However, the redox ability of photogenerated carriers in type-II system is weakened after carriers transfer because the valence band (VB) potential of photocatalyst I (PS I) is more negative than that of photocatalyst II (PS II) and the CB potential of PS II is more positive than that of PS I. How to achieve strong redox ability under the premise of ensuring effective separation of photogenerated carriers has become an important research topic.

In nature, Z-scheme photocatalytic reaction is an important part of photosynthesis in plants, which includes two photochemical reactions and a range of intermediate enzymatic redox reactions (Fig. 1c). Under sunlight, Chlorophyll P680 (PS II) is excited to $P680^*$ (PS II), the electrons in $P680^*$ are transferred to Chlorophyll P700 (PS I) with the help of cytochrome and protease. Then, the electrons in $P700^*$ eventually combines with $NADP^+$ to form NADPH which reduce CO_2 into carbohydrate, and O_2 is produced by water oxidation in P680 (PS II) (Kothe et al., 2013). The artificial Z-scheme photocatalytic systems that mimic natural photosynthesis of plants consist of two suitable bandgap semiconductors, which could simultaneously possess the wide light-absorption range, strong redox ability, and efficient separation efficiency of photogenerated carriers (Deng et al., 2019; Zhang et al., 2019b; Lu et al., 2019). Therefore, the artificial Z-scheme photocatalytic systems excellently solve the problem of easy recombination of photogenerated carriers of single-component photocatalyst and weak redox ability of type-II heterostructure (Deng et al., 2018; Li et al., 2019b; Wang et al., 2020). It is anticipated that constructing silver-based semiconductor Z-scheme photocatalytic systems can not only enhance the photocatalytic activity of silver-based semiconductor photocatalysts, but also improve their stability and reduce the use costs.

Early in 2014, Zhou et al. Zhou et al. (2014) had proposed that the silver-based semiconductors were suitable for the construction of the Z-scheme system. In recent years, many researches have been explored to construct silver-based semiconductor Z-scheme photocatalytic systems to improve their photocatalytic performance. For example, it was reported that $Ag-AgCl/\gamma-TaON$ (Hou et al., 2013a), $Ag/AgX/BiOX$ ($X = Cl, Br$) (Ye et al., 2012), $AgBr/Bi_2WO_6$ (Huang et al., 2019b), $AgI/BiOBr$ (Yu et al., 2018), $Ag_3PO_4/g-C_3N_4$ (Zhou et al., 2017), Ag_2CrO_4-GO (Xu et al., 2015b), $Ag_2CO_3/Ag/WO_3$ (Yuan et al., 2017a), and $Ag_2O/RGO/TiO_2$ (Hu et al., 2017) exhibited high visible light photocatalytic activity and excellent photostability. As the research moves along, increasing instructive reviews have been conducted, such as the summary of functional design and synthesis strategies of Ag_3PO_4 (Li et al., 2019c; Kausor et al., 2020), the application of AgI based heterojunction (Wen et al., 2020a), or the mechanisms of the photocatalytic decomposition of organic molecules of Ag-compound-based semiconductor (Li et al., 2014). However, the current reviews mostly focused on the properties of individual silver-based materials or only on the degradation of organic compounds. Considering the significant advances on silver-based Z-scheme photocatalysts and the vacancy of summarizing these materials, we believe that a comprehensive review on this subject is necessary to accelerate further developments. This review mainly focuses on the construction and synthesis methods of silver-based semiconductor Z-scheme photocatalytic systems and their potential application in environmental restoration and energy conversion. The roles of metallic Ag displayed in silver-based semiconductor Z-scheme photocatalytic systems are discussed. The mechanism and difficult level of these photocatalytic applications, including organic pollutants degradation, H_2 production and CO_2 reduction, are described in detail. Besides, metal organic frameworks (MOFs) as a novel type of photocatalysts have attracted growing attention. The powerful combination of silver-based semiconductors with a typical photoactive MOFs is also highlighted

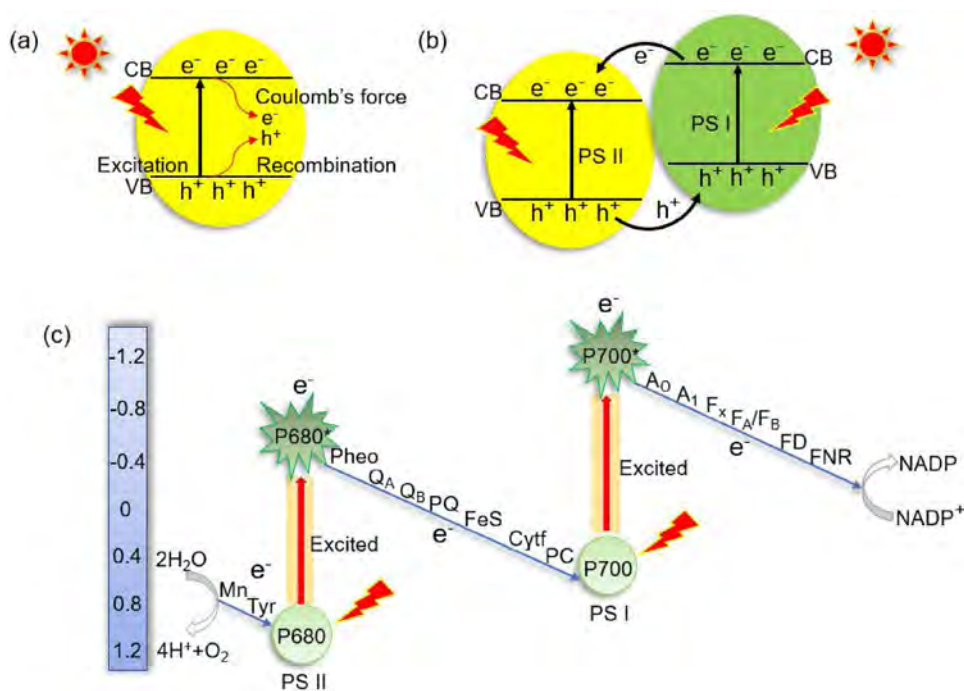


Fig. 1. (a) Electron-hole recombination on a single photocatalyst; (b) Type-II heterojunction; (c) Charge separation mechanism in natural photosynthesis. P680: pigment (chlorophyll) that can absorb 680 nm light in photosystem II (PS II); P680*: the excited state of P680; P700: pigment (chlorophyll) that can absorb 700 nm light in photosystem I (PS I); P700*: the excited state of P700. Mn: manganese-calcium oxide cluster; Tyr: tyrosine in PS II; Pheo: pheophytin, the primary electron acceptor of PS II; Q_A : plastoquinone electron acceptor; Q_B : secondary plastoquinone electron acceptor; PQ: plastoquinone; FeS: Rieske iron-sulfur protein; Cytf: cytochrome f; PC: plastocyanin; A_0 , A_1 : two separate iron-sulfur centers; F_X , F_A , F_B : primary electron acceptors of PS I; FD: ferredoxin; FNR: nicotinamide adenine dinucleotide phosphate (NADP) reductase.

based on the Z-scheme photocatalytic systems. Finally, the future challenges and prospects in the development of silver-based semiconductor Z-scheme photocatalytic systems are presented.

2. The principles of Z-scheme photocatalytic systems

The artificial Z-scheme photocatalytic systems include three types: (1) traditional Z-scheme photocatalytic system, (2) all-solid-state Z-scheme photocatalytic system, and (3) direct Z-scheme photocatalytic system. As shown in Fig. 2a, traditional Z-scheme photocatalytic system consists of two different photocatalysts and redox electron mediators (also called an acceptor/donor (A/D) pair). There is no physical contact between PS II and PS I. Under light irradiation, the electron acceptor (A) is reduced to the electron donor (D) and consumed by the photo-generated electrons in the CB of PS II, while the electron donor (D) is oxidized to the electron acceptor (A) and consumed by the

photogenerated holes in the VB of PS I. Then, the photogenerated hole in the VB of PS II and the photogenerated electron in the CB of PS I can participate in the redox reaction. Although the redox mediators are beneficial to the transmission of electrons between different interfaces, there are also some shortcomings in the process of reaction: First, the presence of redox electron mediators may also absorb light energy, which reduces the photons involved in photocatalytic reactions and is not conducive to photocatalytic reactions; Second, redox electron mediators can react with the photogenerated electrons in the CB of PS I and holes in the VB of PS II, which reduces the number of photo-generated electrons and holes; Third, low stability of redox electron mediators are only suitable for the liquid-phase photocatalytic reactions. These disadvantages above limit its development. Thus, the A/D-free Z-scheme photocatalytic systems gained more attention and development.

As depicted in Fig. 2b, an all-solid-state Z-scheme photocatalytic

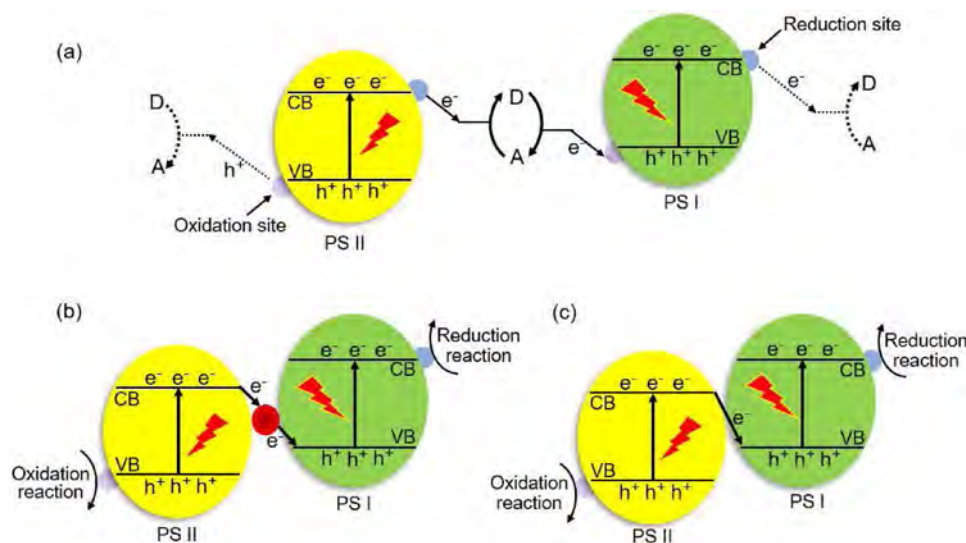


Fig. 2. Schematic illustration of charge transfer in (a) traditional Z-scheme photocatalytic system, (b) all-solid-state Z-scheme photocatalytic system, and (c) direct Z-scheme photocatalytic system.

system is constructed by two different photocatalysts and a solid electron mediator which exists in the contact interface between two semiconductors. Noble metals (e.g., Ag, Au) and conductive materials (e.g., graphene) have been used as the solid electron mediator. Under light irradiation, the photogenerated electrons in the CB of PS II can recombine with the photogenerated holes in the VB of PS I through the solid electron mediator, and achieved highly efficient separation of photogenerated electron-hole pairs and strong redox ability. Notably, the backward reactions of traditional Z-scheme photocatalytic system can be avoided because of the absence of redox mediators. In addition, the all-solid-state Z-scheme photocatalytic system can work both in liquid and gas phases. However, the solid electron mediator may also lead to shielding effect in the all-solid-state Z-scheme photocatalytic system.

A direct Z-scheme photocatalytic system without electron mediator was initially proposed by Yu et al. (Yu et al., 2013). The photogenerated electrons in the CB of PS II can directly recombine with the photogenerated holes in the VB of PS I (Fig. 2c). Compared to traditional and all-solid-state Z-scheme photocatalytic systems, the backward reactions and shielding effect can all be significantly reduced in direct Z-scheme system. Besides, direct Z-scheme photocatalytic system not only can retain high redox ability and efficient carriers separation, but also has a certain corrosion resistance. For example, when silver-based semiconductor photocatalyst as an oxidation component is employed to construct direct Z-scheme system, the photogenerated electrons in the CB of silver-based semiconductor can be rapidly consumed by the photogenerated holes of other photocatalyst, which decrease the possibility of Ag^+ being reduced.

3. The construction of silver-based semiconductor Z-scheme photocatalytic systems

Generally, silver-based semiconductors are a kind of light sensitive materials that tend to be easily reduced to metallic Ag under light irradiation. The roles of metallic Ag in silver-based semiconductor all-solid-state Z-scheme photocatalytic systems mainly focus on two aspects: surface plasmon resonance (SPR) and charge transmission bridge. In addition, some studies have shown that the photocorrosion of silver-based composite semiconductors could be inhibited by consuming the photogenerated electrons timely or transferring the electrons in the CB of silver-based semiconductors to an acceptor material (Xu et al., 2015b; Wan et al., 2017; Li et al., 2016a; Wang et al., 2016a). For example, Xu et al. (Xu et al., 2015b) synthesized a direct Z-scheme silver chromate-graphene oxide (Ag_2CrO_4 -GO) composite photocatalyst, finding that the photostability of Ag_2CrO_4 was significantly enhanced by timely transfer the photogenerated electrons of Ag_2CrO_4 to GO. At present, few reviews have summarized the silver-based semiconductor Z-scheme systems and explored the roles of metallic Ag in there. Therefore, a comprehensive review about this topic is essential for the understands of silver-based semiconductor Z-scheme photocatalytic systems. In the following, we will discuss the two Z-scheme systems of silver-based semiconductor, including all-solid-state Z-scheme systems and direct Z-scheme systems, and analyze the different roles of metallic Ag in all-solid-state Z-scheme photocatalytic systems.

3.1. All-solid-state Z-scheme systems with Ag SPR effect

Theoretically, the SPR of noble metal nanoparticles (NPs) can appear when the frequency of the incident light coincides the natural frequency of the oscillating surface electrons (Fig. 3a). Metallic Ag, as a noble metal NPs, possesses efficient plasmon resonance in visible light region due to the SPR effect, leading to the strong absorption of sunlight (Wang et al., 2011; Xue et al., 2018b). The introduction of plasmonic metals mainly extends the photocatalytic activity of wide bandgap semiconductor material from ultraviolet to visible regions. In silver halide (AgX , X = Cl, I, Br), silver chloride (AgCl) with wide bandgap

($E_g \sim 3.25$ eV) is a photocatalytic material with ultraviolet response, when it coexists with Ag, a plasmonic Z-scheme photocatalytic system using visible light can be constructed (Hou et al., 2013a, b). Wang et al. (Wang et al., 2011) synthesized $\text{Ag}/\text{AgCl}/\text{H}_2\text{WO}_4/\text{H}_2\text{O}$ composite photocatalysts by a one-step ionic method. It was indicated that the Ag NPs formed on AgCl surface increased the visible light absorption ability of composites owing to its SPR effect. Charge carriers transfer in $\text{Ag}/\text{AgCl}/\text{H}_2\text{WO}_4/\text{H}_2\text{O}$ composite was confirmed to obey the plasmonic Z-scheme mechanism. Ag NPs and H_2WO_4 could all absorb photons to generate photogenerated electrons and holes under visible light. The plasmon-induced electrons of Ag NPs were migrated to the CB of AgCl to reduce O_2 , while the photogenerated electrons formed on the CB of H_2WO_4 were entrapped by the plasmon-induced holes of Ag NPs owing to its high Schottky barrier at the interface of Ag and H_2WO_4 . Subsequently, the VB holes on H_2WO_4 oxidize organic pollutants (Fig. 3b). Moreover, plasmonic Z-scheme photocatalytic systems, including $\text{AgCl}/\text{Ag}/\gamma\text{-TaON}$ (Hou et al., 2013a), $\text{Ag-AgCl}/\text{Bi}_{20}\text{TiO}_{32}$ (Hou et al., 2013b), and $\text{Ag}/\text{AgCl}/\text{Bi}_2\text{MoO}_6$ (Jing et al., 2015), have been prepared respectively by Jiao and Niu research group via similar deposition and photo-reduction process. And the improved photocatalytic activity and broadened visible light absorption could be obtained in these plasmonic Z-scheme photocatalytic systems owing to the SPR effect of Ag NPs. Under visible light irradiation, the intrinsic mechanisms for plasmonic enhancement of photocatalysis mainly include local electric field and plasmonic sensitization.

3.1.1. Enhanced local electric field

An intense local electric field near the metal NPs surface can be formed together with the SPR (Fig. 3a). Semiconductor part near plasmonic metal NPs is affected by a strong electric field, which the intensity is 1000 times larger than far-field incident light (Ingram and Linic, 2011; Fei et al., 2008; Xue et al., 2019a). The amount of photogenerated carriers produced in this part of semiconductor is sharply increased because the generation and separation efficiency of photogenerated electron-hole pairs are proportional to the electric field intensity (Fig. 3c). The enhanced local electric field induced by plasmon excitation declines almost exponentially from the surface of metal NPs and extends to 10–50 nanometers according to the size and shape of metal NPs (Tian et al., 2012). Only within this special scale, the generation efficiency of photogenerated electron-hole pairs in semiconductors can be increased. In order to maximize the SPR-induced enhancement of light absorption in semiconductors, it is necessary to achieve complete spectral overlap among semiconductor absorption, incident excitation light and SPR of metal NPs, and increase the effective contact interface between metal and semiconductor.

3.1.2. Plasmonic sensitization

Plasmonic sensitization is electron transfer process that occurs at the interface of metal and semiconductor (Fig. 3d). Most semiconductors used for photocatalysis are n-type. There exists a Schottky barrier between metal and semiconductor in their composites, which prevents the transfer of electrons from metal to semiconductor. Yet, under the excitation of the SPR, the hot electron-hole pairs at metal NPs surface can generate during the decline of the plasmon quantum through non-radiative Landau damping (Meng et al., 2016; Maier et al., 2003). The partially generated hot electrons have enough energy to overcome the Schottky barrier, and can be moved to the CB of semiconductors, driving the chemical reaction. Therefore, due to the process of plasmonic sensitization, the wide bandgap semiconductor material could obtain extra electrons under visible light irradiation. It is also noteworthy that the injection of hot electrons can be influenced by the size, shape, and properties of metal particles and the adjacent semiconductors.

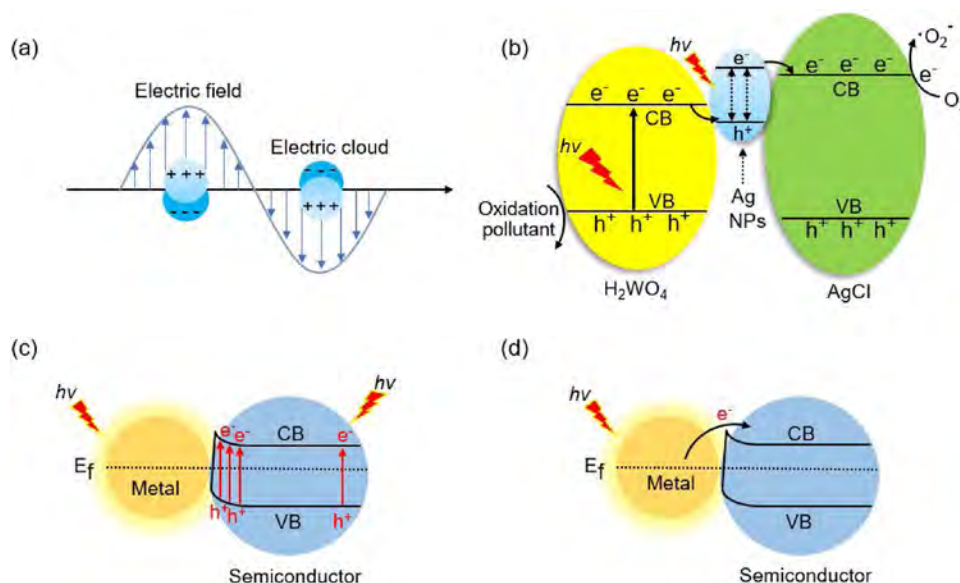


Fig. 3. (a) Schematic illustration of the SPR effect of metal NPs; (b) Plasmonic Z-scheme mechanism of Ag/AgCl/H₂WO₄/H₂O; (c) Plasmonic enhancement of light absorption; (d) Plasmonic sensitization.

3.2. All-solid-state Z-scheme systems with Ag as charge transmission bridge

Besides the SPR effects, the Ag NPs formed on the surface of silver-based semiconductor can be used as charge transmission bridge to facilitate photogenerated carriers separation in silver-based semiconductor Z-scheme systems, because the Fermi level of noble metals is usually lower than the CB potential of semiconductors. Ren et al. [Ren et al. \(2018\)](#) successfully fabricated a Z-scheme AgI/Ag/Bi₃TaO₇ photocatalyst using an ultrasonic-assisted precipitation-photoreduction method and found it displayed superior photocatalytic activity for sulfamethoxazole degradation. The transfer pathway of photogenerated carriers was presented in [Fig. 4a](#). Under visible light irradiation, AgI and Bi₃TaO₇ could be excited to generate electron-hole pairs. The photogenerated electrons formed on the CB of Bi₃TaO₇ could move to Ag NPs through Schottky barrier due to the more positive Fermi level of Ag than the CB potential of Bi₃TaO₇. At the same time, the electrons on Ag NPs surface quickly shift to the VB of AgI because the Fermi level of Ag was more negative than the VB potential of AgI. Then, the separation of photogenerated carriers and strong redox ability were realized. The above charge transfer way also confirmed that Ag NPs as the charge transfer bridge played a crucial role in this system. In another study, an in-situ precipitation procedure was adopted to synthesize the Z-scheme Ag₃PO₄/In₂S₃ photocatalyst, which anchored Ag₃PO₄ on In₂S₃ hierarchical microspheres [\(Yan et al., 2017\)](#). The boosted photocatalytic activity of this catalyst was attributed to the efficient separation of photogenerated carriers through a Z-scheme system, in which a small amount of reducible Ag NPs acted as the charge transfer bridge.

Furthermore, the presence of Ag NPs can enhance the photostability of silver-based semiconductor owing to the reason that Ag act as electron acceptors to trap photogenerated electrons in silver-based semiconductor, avoiding the direct reduction of Ag⁺. Also, AgI/BiVO₄ [\(Chen et al., 2016\)](#), CeO₂-Ag/AgBr [\(Wen et al., 2018b\)](#), Ag₂CrO₄/Ag/g-C₃N₄ [\(Gong et al., 2017\)](#), and Ag₃PO₄/g-C₃N₄ [\(He et al., 2015\)](#) were constructed with similar mechanism. So, how to distinguish the different role of Ag NPs in silver-based semiconductor Z-scheme photocatalytic systems? Generally, when PS II or PS I is photoexcited, the SPR effect of Ag NPs plays significant role. When both PS II and PS I are photoexcited, the Ag NPs mainly act as charge transmission bridge. However, when both PS II and PS I cannot be photoexcited, Ag NPs possess SPR effects but the reaction system is not Z-scheme. [Ye et al. \(2012\)](#) prepared two kinds of Ag/AgCl/BiOCl and Ag/AgBr/BiOBr photocatalysts and explored the role of Ag in two systems. The absorption edges of AgCl, AgBr, BiOCl, and BiOBr were 382, 477, 358, and 428 nm, respectively. Thus, AgCl and BiOCl cannot be excited under visible light irradiation. The enhanced photocatalytic performance of the Ag/AgCl/BiOCl composite was only ascribed to the SPR of metallic Ag. In addition, the generated C¹ was another active species in photodegradation reaction. Under visible light irradiation, AgBr and BiOBr were excited, and the CB electrons of BiOBr flow into Ag through the Schottky barrier because the CB potential of BiOBr was more negative than that Fermi level of the loaded Ag. On the other hand, since the Fermi level of Ag is more positive than the VB of AgBr, the VB holes of AgBr also flow into Ag. Therefore, the role of Ag was only the Z-scheme bridge for Ag/AgBr/BiOBr system because of the visible light response

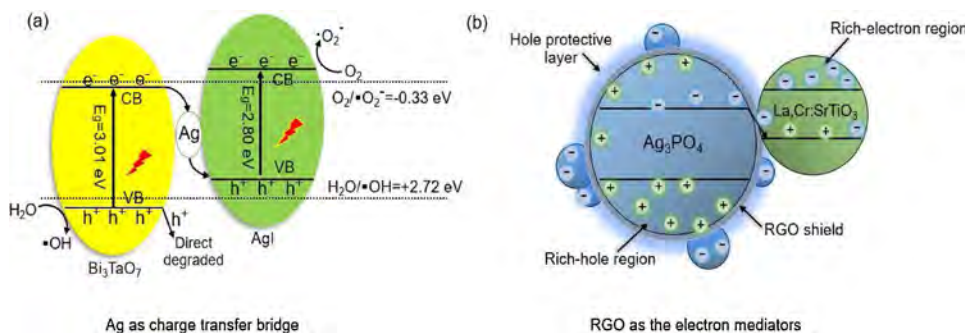


Fig. 4. (a) Schematic illustration of the charge separation of AgI/Ag/Bi₃TaO₇; (b) Photocorrosion-inhibition mechanism of Ag₃PO₄@RGO@La,Cr:SrTiO₃.

of AgBr and BiOBr. It shows that Ag can improve the photocatalytic performance not only for narrow bandgap photocatalyst ($E_g < 3.1$ eV) but also for wide bandgap photocatalyst ($E_g > 3.1$ eV) through different roles it displayed. Similar results could also be reported by Wen et al. Wen et al. (2019).

In short, Ag NPs can not only extend the light absorption spectrum but also suppress the recombination of electron-hole pairs and reduce the occurrence of photocorrosion of silver-based semiconductor. Thus, loading Ag NPs on the surface of photocatalysts has provided a new approach to overcome the restricted efficiency of silver-based semiconductor. However, the loading of excessive metal particles will not only occupy the active sites of photocatalyst, but also reduce the light absorption, so the number of metal particles loaded should be further studied.

Besides Ag, reduced graphene oxide (RGO) with large surface area, excellent conductivity, special layered structure and high chemical stability can also be employed as the electron mediators. The Z-scheme $\text{Ag}_3\text{PO}_4/\text{RGO}/\text{La,Cr:SrTiO}_3$ photocatalyst with RGO as the electron mediators was synthesized by Cai et al. Cai et al. (2017). It was demonstrated that RGO packaged on Ag_3PO_4 surface could timely transport electrons away from Ag_3PO_4 and consumed by the holes generated in the VB of La,Cr:SrTiO_3 , leading to the effective separation of photogenerated carriers and a rich-hole region in Ag_3PO_4 surface. And the rich-hole micro-environment could protect Ag_3PO_4 from photoreduction (Fig. 4b). Besides, Zhang et al. Zhang et al. (2020) reported a two-step process for the synthesis of CdS/AgBr-rGO (CAR) composite photocatalysts. They revealed that the composite exhibit higher activity for the organic pollutants. The electrochemical analysis demonstrated that CdS and AgBr formed a Z-scheme photocatalytic system via RGO at the interface of the two semiconductors acting as a solid electron shuttle where the photogenerated electron-hole pairs were efficiently separated through electron transfer. It is expected that the introduction of RGO is an efficient way to improve the properties of silver-based semiconductor Z-scheme systems. Significantly, effective conduction of RGO can enhance the electron transfer, which can inhibit the photocorrosion by preventing the reduction of Ag^+ to Ag^0 .

3.3. Direct Z-scheme systems

As discussed in Section 2, direct Z-scheme photocatalytic system not only can maintain strong redox ability, but also has a certain corrosion resistance owing to the photogenerated electrons formed on the CB of silver-based semiconductor can be timely consumed by the other semiconductors. Many studies have been conducted to enhance the photostability of silver-based semiconductors by constructing direct Z-scheme system with other semiconductor materials (Yu et al., 2018; Xu et al., 2015b; Wan et al., 2017; Tan et al., 2017; Wang et al., 2016b; Bing et al., 2017; Deng et al., 2016; Zhang et al., 2015; Yin et al., 2020; Zhang et al., 2019c; Ke et al., 2019; Lu et al., 2017; Wen et al., 2020b; Guo et al., 2018c). Specially, a novel Ag_3PO_4 NPs @ MoS_2 quantum dot/ MoS_2 nanosheet core@shell heterostructure was prepared through the stirring-ultrasonic exfoliation reaction and a succedent organic phase in-situ growth procedure (Wan et al., 2017). Quantum dots are formed in the ultrasonic process of bulk MoS_2 and loaded on MoS_2 nanosheet and used as shell together. Fig. 5a indicated the atomic force microscope (AFM) image of MoS_2 nanosheet with precise nanometer thicknesses of sections A and B were 1.894 and 3.703 nm, confirming the successful construction of MoS_2 nanosheets. Ag_3PO_4 NPs was covered closely by few-layer MoS_2 nanosheets to form core@shell structure (Fig. 5b), which could protect Ag_3PO_4 NPs from photocorrosion in the photocatalytic reaction and promote the separation of photogenerated carriers at their interface. Results showed that the composites exhibited excellent stability after five cyclic experiments, and the superior photocatalytic performance of the composites derives from the direct Z-scheme carriers transfer pathway (Fig. 5c) and the core@shell structure of composite. It may be a good strategy to construct core@shell

structure photocatalysts for improving the photostability of the silver-based semiconductor core based on the Z-scheme mechanism. Zhang et al. (Wang et al., 2016b) fabricated a visible-light-driven AgI/WO_3 nanocomposite via in-situ precipitation method. The optimum photocatalytic performance for tetracycline (TC) photodegradation over 20 % AgI/WO_3 was about 4.3 and 25 times high as that of pure AgI and WO_3 , respectively. The possible mechanism for the enhanced photocatalytic activity could be attributed to the formation of a direct Z-scheme system which causes the photogenerated electrons migrate from WO_3 to AgI, leading to effective charge separation of WO_3 . As we discussed earlier, pure silver-based semiconductors is unstable because the Ag^+ may be reduced into Ag^0 species during the photocatalytic process. Worth noting that, the stability of silver-based semiconductors can be enhanced when the direct Z-scheme system with other semiconductor have been constructed successfully. More efforts should be done to construct the silver-based semiconductor direct Z-scheme photocatalytic system to further inhibit the photocorrosion of silver-based semiconductors.

4. Synthesis methods of silver-based semiconductor Z-scheme photocatalytic systems

4.1. Precipitation method

The precipitation method is a traditional and facile method for the preparation of silver-based semiconductor Z-scheme photocatalysts. Generally, this method is carried out by mixing the synthesized semiconductor materials with the raw materials of silver-based semiconductor and reacting for a certain time to form the required precipitate (Zhou et al., 2017; Xu et al., 2015b; Hu et al., 2017; Yan et al., 2017; Chen et al., 2016; Tan et al., 2017; Wang et al., 2016b; Deng et al., 2016; Zhang et al., 2015; Yin et al., 2020; Guo et al., 2018c; Chen et al., 2017a). If the resulting suspension is exposed to visible light, Ag NPs will be produced, which can be defined the precipitation-photoreduction process (Hou et al., 2013a; Yuan et al., 2017a; Jing et al., 2015; Wen et al., 2018b; Gong et al., 2017; He et al., 2018; Liang et al., 2019). For example, the Z-scheme $\text{Ag}/\text{AgCl}/\text{Bi}_2\text{MoO}_6$ system was accomplished by irradiating the two-component $\text{AgCl}/\text{Bi}_2\text{MoO}_6$ composite with Xe lamp for 30 min (Jing et al., 2015). The Ag NPs were in-situ generated in the contact interface between AgCl and Bi_2MoO_6 . When AgI was substituted for BiVO_4 , the Ag NPs could be still in-situ generated under light irradiation. The resulting $\text{AgI}/\text{Ag}/\text{BiVO}_4$ system shows the similar Z-scheme electron transfer as the former one (Chen et al., 2016). In addition, the photocatalytic performance of the composite could be affected by the ratio of silver to the composite (Chen et al., 2016; Wen et al., 2018b). A Z-scheme $\text{CeO}_2/\text{Ag}/\text{AgBr}$ hybrids with different Ag mass ratios of 5.12, 13.94, 21.26 and 27.43 wt% (denoted as CAB-5.12, CAB-13.94, CAB-21.26 and CAB-27.43) were reported by Wen et al. (Wen et al., 2018b). Ag/AgBr was loaded onto the surface of CeO_2 via precipitation-photoreduction process. The elimination efficiency of ciprofloxacin could reach 65.12, 87.32, 93.05, and 80.29 % for CAB-5.12, CAB-13.94, CAB-21.26, and CAB-27.43, respectively, within 120 min of visible light irradiation. Characterization data indicated that CAB-21.26 hybrids composites exhibited higher photogenerated charge separation efficiency.

4.2. Ion exchange method

Ion exchange method is realized by the diffusion between the free flowing ions carried by the synthesized semiconductor materials and the ions in the treated solution. This method is one of widely adopted to fabricate silver-based semiconductor Z-scheme photocatalytic systems. The operation condition is simple and the cost is low. The two semiconductors in the silver-based semiconductor Z-scheme photocatalytic systems constructed by ion exchange method are generally silver based semiconductors (Cai et al., 2019; Hu et al., 2015; Chen et al., 2013;

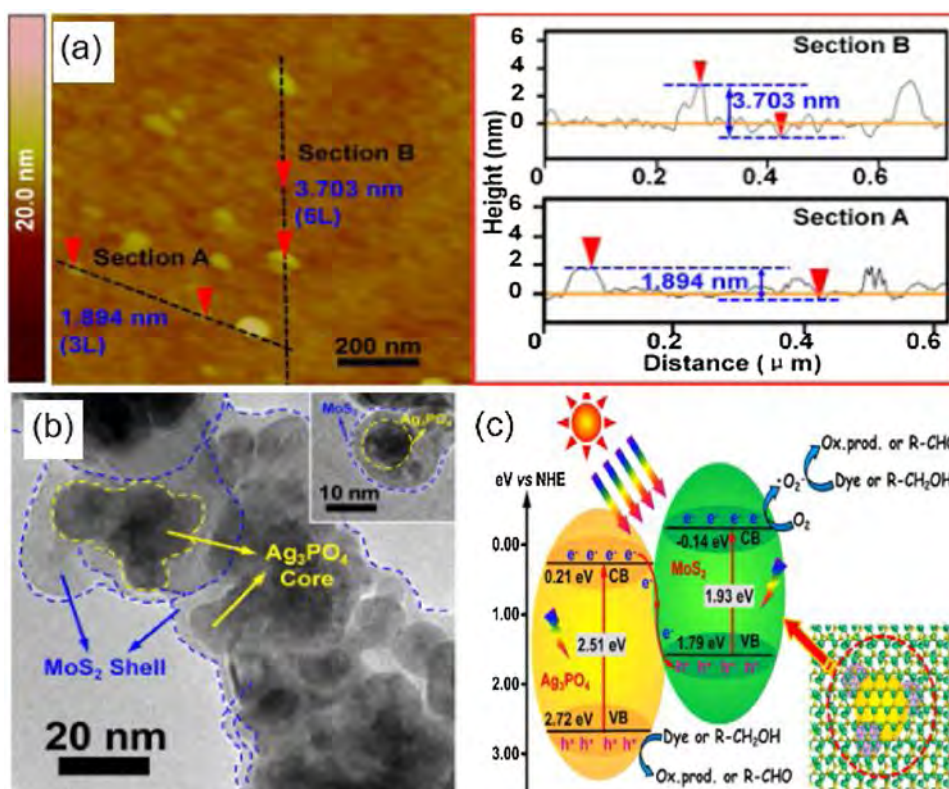


Fig. 5. (a) AFM image and corresponding height profile of MoS₂ nanosheets; (b) TEM images of as-prepared MoS₂-Ag₃PO₄ nanocomposite; (c) Schematic illustration of the photocatalytic mechanism of composites under visible light irradiation. Reproduced with permission from Ref. Wan et al. (2017). Copyright 2016 Elsevier.

Wang et al., 2016c; Lin et al., 2012). Chen et al. (2013) prepared Z-scheme Ag₃PO₄/AgI photocatalysts with different mole fractions of AgI via an in-situ anion exchange method. Compared with pure Ag₃PO₄ or AgI, the Ag₃PO₄/AgI-20 % composite exhibited enhanced photocatalytic activity for the degradation of MO and phenol. In this system, Ag₃PO₄ was utilized as Ag⁺ ion sources instead of AgNO₃, and then different amounts of sodium iodide solution were dropped into the Ag₃PO₄ dispersion. Similarly, AgI/AgVO₃ nano-ribbon composites were synthesized via a facile in-situ ion exchange approach (Wang et al., 2016c). The improvement in the photocatalytic redox properties of AgI/AgVO₃ was mainly ascribed to the efficient separation of photogenerated electrons/holes via a Z-scheme bridge mechanism of formed Ag/AgI/AgVO₃, in which Ag nanoparticles serve as the charge migration bridge.

4.3. Hydrothermal method

Hydrothermal preparation of silver-based semiconductor Z-scheme photocatalytic system is also a noteworthy method. It is utilizing the chemical reaction between the reagents under specific temperature and pressure (Shi et al., 2013). The operating parameters such as synthesis temperature, synthesis time and precursor concentration are easy to adjust (Zhang et al., 2020; Lu et al., 2017; Zhu et al., 2016b). At the same time, the surrounding atmosphere is easy to control under hydrothermal condition, which is conducive to the formation of intermediate and special valence compounds, and can realize the binding process uniformly. Lu et al. (2017) prepared a direct Z-scheme WO₃/Ag₃PO₄ photocatalyst by hydrothermal method. Results showed that the large size of Ag₃PO₄ would be due to the relatively high hydrothermal temperature in the hydrothermal process. The particle size of WO₃ was relatively uniform. Compared with pure Ag₃PO₄ and WO₃, the composite exhibited notably enhanced photocatalytic efficiency. It was also revealed that the developing of 1 W/1Ag not only improved the reaction activity, but also effectively reduced the cost of the Ag₃PO₄

based Z-scheme photocatalyst. However, compared to precipitation and ion exchange methods, this method is time-consuming and not suitable for mass production.

4.4. Others

Besides the methods discussed above, there are also some other methods to prepare silver-based semiconductor Z-scheme photocatalyst. For example, Li et al. (2015b) synthesized a Z-scheme photocatalyst Ag@AgCl/BiVO₄ composite by photoreduction and in-situ oxidation. First, the Ag/BiVO₄ sample was prepared via photoreduction. Second, the Ag@AgCl/BiVO₄ composite was prepared by an in-situ oxidation reaction between Ag/BiVO₄ and FeCl₃ aqueous solution. Finally, the Ag@AgCl core-shell structure was decorated on the crystal facet of BiVO₄ as a hierarchical Z-scheme photocatalytic system. In this hybridization system, the Ag NPs could both act as the solid state electron mediator and enhance the visible light absorption corresponding with SPR-effect. A graphitic-C₃N₄-hybridized Ag₃PO₄ tetrahedron with reactive {111} facets (Z-scheme system) was prepared through a ultrasonication and solvent evaporation procedure (Tang et al., 2015). It was showed that the g-C₃N₄ assembled on the surface of Ag₃PO₄ or gathered around Ag₃PO₄ to achieve a minimum surface energy during ultrasonication and ethanol evaporation process.

At present, most of the silver-based semiconductor Z-scheme photocatalysts are prepared in the laboratory. Silver-based semiconductor materials are sensitive to light, and the laboratory light is likely to reduce Ag⁺ and produce Ag NPs. Previous study had showed that the prepared AgBr microspheres were irradiated under sunlight, the Ag⁺ on the surface of the microspheres were reduced (Kuai et al., 2010). Therefore, in order to avoid the possible negative effects of the laboratory light on the material synthesis process, most of the preparation of silver-based semiconductor Z-scheme photocatalysts are basically completed in the dark.

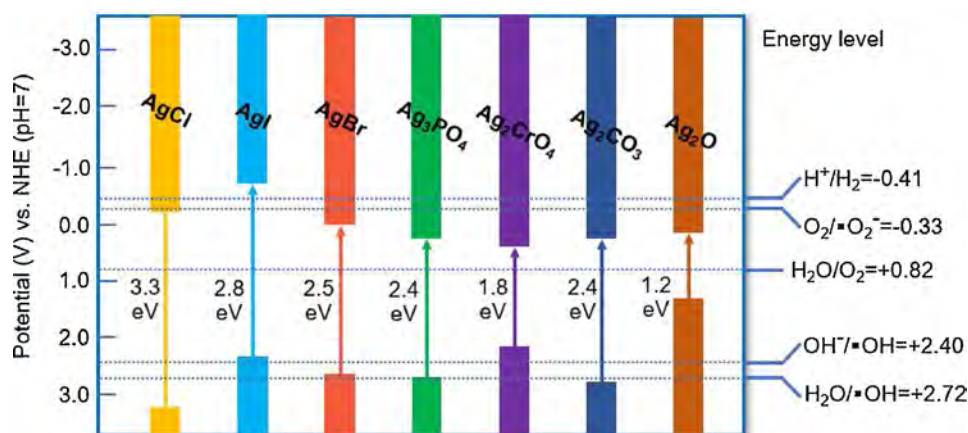


Fig. 6. Energy band diagram of some representative silver-based semiconductor materials.

5. Photocatalytic processes

Silver-based semiconductor materials are one of the most widely studied photocatalytic materials driven by visible light at present, mainly including AgX (X = Cl, I, Br), Ag_3PO_4 , Ag_2CrO_4 , Ag_2CO_3 , and Ag_2O (all energy band potentials vs. NHE, pH = 7 are depicted in Fig. 6). The synthesis processes, photocatalytic activities and morphologies of these Ag-based semiconductor photocatalysts were summarized in the Supporting Information (Table S1). Combining silver-based semiconductor materials and other semiconductor to construct a composite Z-scheme photocatalytic system can improve the photocatalytic activity, stability and cost reduction of silver-based semiconductors, thus contributing to promote the practical application of silver-based materials in new energy utilization and environmental decontamination. In this section, a range of photocatalytic-involved applications, including organic pollutant degradation, H_2 generation, CO_2 reduction, are presented. Meanwhile, the reaction mechanism and difficult level of these photocatalytic reactions are also described in detail.

5.1. Photodegradation of organic pollutants

5.1.1. Reaction mechanisms

Artificial Z-scheme photocatalytic system usually composes of two connected photocatalysts: one is an oxidative photocatalyst and the other is reductive photocatalyst. For example, Ag_3PO_4 is an oxidative photocatalyst with low VB potential and possess high oxidation ability, which usually combined with high CB semiconductor material to construct Z-scheme photocatalytic system (Wan et al., 2017; Cai et al., 2017; Tan et al., 2017; Shi et al., 2017; Lin et al., 2015; Meng et al., 2015). Under visible light irradiation, charge carriers transfer via electron mediator (Ag, GO, etc.) or direct transfer at composites interface to surface active sites. Then, the photogenerated electrons on one semiconductor (PS I) with high CB could reduce O_2 to generate $\cdot\text{O}_2^-$ if the CB potential is negative than $\text{O}_2/\cdot\text{O}_2^-$ potential (-0.33 V vs. NHE). The photogenerated holes on other semiconductor (PS II) with low VB could oxidize OH^- or H_2O to produce $\cdot\text{O}^\cdot\text{H}$ or direct oxidation of organic pollutants if the VB potential is positive than the potential of $\text{O}^\cdot\text{H}/\text{OH}^-$ (+2.40 V vs. NHE) or $\text{H}_2\text{O}/\text{O}^\cdot\text{H}$ (+2.72 V vs. NHE) (Shao et al., 2018a; Jiang et al., 2018a; Wang et al., 2018; Gong et al., 2018). Thus, the generated $\cdot\text{O}_2^-$, $\cdot\text{O}^\cdot\text{H}$, and holes could effectively oxidize the organic pollutants to smaller molecules or decompose them into CO_2 and H_2O . The photocatalytic reaction mechanism above is applicable to Ag as a charge transmission bridge or direct Z-scheme system. In addition, if the enhancement of photocatalytic performance of composite materials is mainly due to the SPR effect of metallic Ag, the reaction mechanisms obey the plasmonic Z-scheme mechanism. As described in

above, the introduction of plasmonic metals is mainly to enhance the photocatalytic performance of wide bandgap semiconductor material, because the excitation energy of SPR is usually lower than that of semiconductor. For silver-based semiconductor, Ag/AgCl can combined with a variety of visible light response photocatalytic materials to form plasmonic Z-scheme system. The reaction mechanism of plasmonic Z-scheme photocatalytic system can be summarized as follows: under visible light irradiation, the plasmon-induced electrons of Ag NPs are transferred to the CB of AgCl to reduce O_2 . Simultaneously, the plasmon-induced holes left on the Ag NPs are recombined with the photogenerated electron from another excited semiconductor to effectively facilitate the photogenerated carrier separation in semiconductor, while the photogenerated holes left on semiconductor to oxidize organic pollutants.

5.1.2. Application

Based on these functional mechanisms, many silver-based semiconductor Z-scheme photocatalysts with different geometrical configurations and compositions, have been extensively synthesized and applied in photodegradation of organic pollutants. Tables 1 and 2 summarizes the recent studies of some representative silver-based Z-scheme photocatalysts for organic pollutants degradation. In the following, we will select some well-designed photocatalyst as examples to explain the applications of silver-based semiconductor Z-scheme photocatalysts in organic pollutants degradation.

5.1.2.1. Photodegradation of aqueous organic pollutants. The photocatalytic activity of a specific semiconductor highly depends on the crystal facet properties owing to the different mobility of photogenerated carriers and energy band levels in different crystal facet of semiconductor (Li et al., 2015b; Tang et al., 2015; Cai et al., 2019; Yin et al., 2018). Previous studies showed that the (040) crystal facets of BiVO_4 had high charge mobility and photocatalytic active sites (Li et al., 2013; Kim et al., 2016). Li et al. (Li et al., 2015b) constructed a plasmonic Z-scheme photocatalyst by decorating core-shell structure Ag@AgCl on the (040) crystal facet of BiVO_4 (Fig. 7a and b), and the obtained catalyst exhibited higher photocatalytic performance for RhB degradation. The UV-vis diffuse reflectance spectra (DRS) of catalysts were presented in Fig. 7c. It was observed that the Ag/ BiVO_4 displayed a better light absorption ability than the others, which was attributed to the SPR effect of Ag. Moreover, the photocurrent intensity of Ag@AgCl/ BiVO_4 under visible light was stronger than that of BiVO_4 , indicating that the Z-scheme heterojunction system of Ag@AgCl/ BiVO_4 with Ag plasmonic sensitization effect could effectively boost the separation of photogenerated carriers (Fig. 7f). In addition, some other plasmonic metal NPs based Z-scheme photocatalysts have been reported for the photocatalytic degradation of aqueous organic pollutants. The catalytic

Table 1
Summary of representative AgX (X = Cl, I, Br)-based Z-scheme photocatalysts for degradation of organic pollutants.

Catalyst	Synthesis method	Electron mediator	Target (concentration)	Catalyst dose (g/L)	Light source	Activity (reference activity)	Ref.
Ag@AgCl/BiVO ₄ (040)	Photooxidation and in-situ oxidation	Ag	RhB (10 mg/L)	2	500 W Xe lamp ($\lambda \geq 420$ nm)	0.12 min ⁻¹ (BiVO ₄ : 0.0004 min ⁻¹)	(Li et al., 2015b)
Ag/AgCl/Bi ₂ MoO ₆	Precipitation-photoreduction	Ag	RhB (10 mg/L)	1	500 W Xe lamp ($\lambda \geq 420$ nm)	0.039 min ⁻¹ (Bi ₂ MoO ₆ : 0.004 min ⁻¹)	(Jing et al., 2015)
Ag@AgCl/Bi ₂ WO ₆	Hydrothermal treatment and in-situ oxidation	Ag	BPA (2 mg/L)	0.2	500 W high pressure xenon long-arc lamp	0.02473 min ⁻¹ (Bi ₂ WO ₆ : 0.00615 min ⁻¹)	(Zhu et al., 2016b)
Ag-AgCl/ γ -TaON	Deposition and photoreduction	Ag	RhB and acid orange 7 (AO7) solution (1×10^{-4} M, 100 mL)	1	300 W Xe lamp ($\lambda > 420$ nm)	RhB: 96.6 % degraded within 140 min; AO7: 98.0 % degraded within 100 min	(Hou et al., 2013a)
Ag/AgCl/AgFeO ₂	Precipitation	Ag	RhB (10 mg/L)	0.5	300W Xe lamp	0.05861 min ⁻¹ (AgFeO ₂ : 0.00136 min ⁻¹)	(Song and He, 2017)
Ag/AgCl/g-C ₃ N ₄	In-situ oxidation	Ag	MO (10 mg/L)	1	300 W Xe lamp with a 400 nm cut-off filter	0.085 min ⁻¹ (g-C ₃ N ₄ : 0.579 min ⁻¹)	(Teng et al., 2014)
Ag/AgCl/WO ₃	Ultrasonic precipitation	Ag	4-Aminobenzoic acid (10 mg/L)	0.6	300 W Xe lamp with a 420 nm cut-off filter	0.0427 min ⁻¹ (WO ₃ : 0.0017 min ⁻¹)	(Li et al., 2018)
Ag/AgCl/Ag ₂ O	In-situ growth	Ag	CIP (10 mg/L)	1	250 W Xe lamp with a 420 nm cut-off filter	91.2 % degraded, (efficiency was about 2.9 times higher than Ag ₂ O)	(Yang et al., 2017)
AgI/BiVO ₄	In-situ precipitation	Ag	TC (20 mg/L)	0.3	300 W Xe lamp ($\lambda > 420$ nm)	0.0527 min ⁻¹ (BiVO ₄ : 0.0182 min ⁻¹)	(Chen et al., 2016)
Ag@AgI/BiOI	In-situ grown	Ag	TC (20 mg/L)	0.3	300 W Xe lamp ($\lambda > 420$ nm)	0.0317 min ⁻¹ (BiOI: 0.0044 min ⁻¹)	(Yang et al., 2018)
AgI/Bi ₅ O ₇	Deposition-precipitation	Ag	TC (20 mg/L)	0.5	300 W Xe lamp with a 400 nm cut-off filter	0.0922 min ⁻¹ (Bi ₅ O ₇ : 0.0107 min ⁻¹)	(Chen et al., 2017a)
G-AgI/Ag ₃ PO ₄	Chemical coprecipitation	Ag	CBZ (5 mg/L)	0.3	500 W Xe lamp with a 420 nm cut-off filter	0.161 min ⁻¹ (Ag ₃ PO ₄ : 0.016 min ⁻¹)	(Duan et al., 2019)
AgI/AgVO ₃	In-situ ion exchange	Ag	Benzylamine (0.25 mmol)	5	300 W Xe lamp with a 400 nm cut-off filter	> 95 % oxidized for benzylamine (12 h); (AgVO ₃ : 10.5% oxidized for benzylamine)	(Wang et al., 2016c)
AgI/BiOBr	Solothermal-precipitation	-	CIP (10 mg/L)	0.5	300 W Xe lamp with a 420 nm cut-off filter	0.04048 min ⁻¹ (BiOBr: 0.01472 min ⁻¹)	(Yu et al., 2018)
AgI/WO ₃	Precipitation	-	TC (35 mg/L)	1	300 W Xe lamp ($\lambda \geq 420$ nm)	0.0235 min ⁻¹ (WO ₃ : 0.0009 min ⁻¹)	(Wang et al., 2016b)
AgI/ β -Bi ₂ O ₃	Precipitation	-	MO (10 mg/L)	0.5	300 W Xe lamp with a 420 nm cut-off filter	0.0128 min ⁻¹ (β -Bi ₂ O ₃ : 0.00309 min ⁻¹)	(Zhang et al., 2015)
AgI/Bi ₄ V ₂ O ₁₁	Hydrothermal process and in-situ coprecipitation	-	SMZ (10 mg/L)	1	300 W Xe lamp with a 420 nm cut-off filter	0.0431 min ⁻¹ (Bi ₄ V ₂ O ₁₁ : 0.0030 min ⁻¹)	(Wen et al., 2020b)
AgI/Bi ₂ Sn ₂ O ₇	In-situ deposition-precipitation	-	TC (20 mg/L)	1	300 W Xe lamp with a 420 nm cut-off filter	0.0361 min ⁻¹ (Bi ₂ Sn ₂ O ₇ : 0.0110 min ⁻¹)	(Guo et al., 2018c)
ZnFe ₂ O ₄ /AgBr/Ag	In-situ precipitation and photoreduction	Ag	MO (7 mg/L)	0.4	300 W Xe lamp ($\lambda > 420$ nm)	0.0882 min ⁻¹ (ZnFe ₂ O ₄ : 0.0005 min ⁻¹)	(He et al., 2018)
CeO ₂ -Ag/AgBr	In-situ precipitation and photoreduction	Ag	CIP (10 mg/L)	1	300 W Xe lamp with a 420 nm cut-off filter	0.02111 min ⁻¹ (CeO ₂ : 0.00007 min ⁻¹)	(Wen et al., 2018b)
AgBr/Ag/PbBiO ₂ Br	CTAB-assisted calcination	Ag	RhB (10 mg/L); BPA (10 mg/L)	1	300 W Xe lamp with a 420 nm cut-off filter	0.1893 min ⁻¹ for RhB; 0.0134 min ⁻¹ for BPA (PbBiO ₂ Br: 0.0241 min ⁻¹ for RhB; 0.0038 min ⁻¹ for BPA)	(Guo et al., 2018b)
Ag/AgBr/BiOBr	Low-temperature chemical bath	Ag	RhB (10 mg/L)	0.2	500 W Xe lamp ($\lambda \geq 400$ nm)	0.1524 min ⁻¹ (BiOBr: 0.0140 min ⁻¹)	(Ye et al., 2012)
AgBr/MoO ₃	Oriented diffusing and charge induced deposition	-	RhB (10 mg/L)	0.2	250 W Xe lamp	0.468 min ⁻¹ (AgBr: 0.213 min ⁻¹)	(Bing et al., 2017)
AgBr/ β -Ag ₂ WO ₄	Precipitation	-	RhB (10 mg/L)	0.6	300 W Xe lamp with a 420 nm cut-off filter	0.05166 min ⁻¹ (β -Ag ₂ WO ₄ : 0.00038 min ⁻¹)	(Yin et al., 2020)
BON-Br-AgBr	Hydrothermal-precipitation method	-	RB-19 (50 mg/L)	0.6	800 W Xe lamp	0.04421 min ⁻¹ (BON-Br: 0.00524 min ⁻¹)	(Zhang et al., 2019c)
CdS/AgBr-RGO	In-situ precipitation and hydrothermal procedure	RGO	RhB (50 μ mol/L)	0.6	500 W Xe lamp with a 420 nm cut-off filter	0.051 min ⁻¹ (CdS: 0.026 min ⁻¹)	(Zhang et al., 2020)

RhB, Rhodamine B; MO, Methylene Orange; CIP, Ciprofloxacin; TC, Tetracycline; BPA, Bisphenol A; CTAB, Cetyltrimethylammonium bromide; BON, Bi₂O₃(OH)(NO₃); RB-19, Reactive Blue 19; SMZ, Sulfamethazine; CBZ, Carbamazepine.

Table 2
Summary of representative Ag₃PO₄, Ag₂CrO₄, Ag₂CO₃, and Ag₂O-based Z-scheme photocatalysts for degradation of organic pollutants.

Catalyst	Synthesis method	Electron mediator	Target (concentration)	Catalyst dose (g/L)	Light source	Activity (reference activity)	Ref.
Ag ₃ PO ₄ (111)/g-C ₃ N ₄	Ultrasonication and solvent evaporation	Ag	MB (10 mg/L)	0.8	300 W Xe lamp with a 400 nm cut-off filter	0.3412 min ⁻¹ (g-C ₃ N ₄ : 0.0397 min ⁻¹)	(Tang et al., 2015)
Ag ₃ PO ₄ (100)/Ag/AgI	In-situ anion exchange	Ag	RhB (20 mg/L)	0.6	300 W Xe lamp (λ > 420 nm)	0.44 min ⁻¹ (sphere Ag ₃ PO ₄ : 0.06 min ⁻¹ ; cube Ag ₃ PO ₄ : 0.08 min ⁻¹)	(Cai et al., 2019)
Ag ₃ PO ₄ /g-C ₃ N ₄	In-situ precipitation	Ag	SMX (5 mg/L)	0.25	300 W Xe lamp (λ > 400 nm)	0.063 min ⁻¹ (g-C ₃ N ₄ : 0.003 min ⁻¹)	(Zhou et al., 2017)
Ag ₃ PO ₄ /CuBi ₂ O ₄	In-situ precipitation	Ag	TC (10 mg/L)	0.5	300 W Xe lamp with a 420 nm cut-off filter	0.0201 min ⁻¹ (CuBi ₂ O ₄ : 0.0072 min ⁻¹)	(Shi et al., 2017)
Ag ₃ PO ₄ /MoS ₂	Ethanol-water mixed solvents precipitation	Ag	MB (20 mg/L)	1	35 W Xe arc lamp (λ > 420 nm)	0.06548 min ⁻¹ (MoS ₂ : 0.004 min ⁻¹)	(Zhu et al., 2016a)
Ag ₃ PO ₄ /In ₂ S ₃	Precipitation	Ag	MO, RhB, MB, phenol, and SA (10 mg/L)	1	300 W Xe arc lamp (400 < λ < 800 nm)	~100 % degraded for MO, RhB, MB (7 min), > 50 % degraded for phenol and SA (3 h)	(Yan et al., 2017)
Ag@Ag ₃ PO ₄ /g-C ₃ N ₄ /rGO	Photoreduction assisted precipitation	Ag	BDE-47 (5 mg/L)	0.5	300 W Xe lamp (λ > 420 nm)	0.11635 min ⁻¹ (g-C ₃ N ₄ : 0.00067 min ⁻¹ ; Ag@Ag ₃ PO ₄ : 0.00226 min ⁻¹)	(Liang et al., 2019)
Ag ₃ PO ₄ /AgI	In-situ anion exchange	Ag	MO or Phenol (20 mg/L)	2	500 W Xe lamp with a 420 nm cut-off filter	96.9 % degraded for MO (18 min), > 90 % degraded for phenol (18 min)	(Chen et al., 2013)
Ag ₃ PO ₄ @RGO@La,Cr:SrTiO ₃	Solution method	RGO	RhB (10 mg/L); 2,4-DNP (10 mg/L)	1	300 W Xe lamp (λ > 420 nm)	0.79 min ⁻¹ for RhB; 0.052 min ⁻¹ for 2,4-DNP (Ag ₃ PO ₄ : 0.15 min ⁻¹ for RhB; 0.004 min ⁻¹ for 2,4-DNP)	(Cai et al., 2017)
Ag ₃ PO ₄ /SnSe ₂	In-situ precipitation	-	RhB (10 mg/L)	0.6	300 W Xe lamp with a 400 nm cut-off filter	0.07237 min ⁻¹ (SnSe ₂ : 0.0028 min ⁻¹)	(Tan et al., 2017)
Ag ₃ PO ₄ @MoS ₂ QD/MoS ₂	Stirring-ultrasonic exfoliation and organic phase in-situ growth	-	RhB (10 mg/L)	1	300 W Xe lamp (λ > 420 nm)	0.2697 min ⁻¹ (Ag ₃ PO ₄ : 0.0945 min ⁻¹)	(Wan et al., 2017)
Zn ₃ V ₂ O ₈ /Ag ₃ PO ₄	Two-step solution method	-	MB (50 mg/L)	1	50 W 410 nm LED light	0.0715 min ⁻¹ (Zn ₃ V ₂ O ₈ : 0.0019 min ⁻¹)	(Ke et al., 2019)
WO ₃ /Ag ₃ PO ₄	Hydrothermal method	-	MB (10 mg/L)	1	300 W Xe lamp (λ > 420 nm)	0.048 min ⁻¹ (WO ₃ : 0.0019 min ⁻¹)	(Lu et al., 2017)
Ag ₂ CrO ₄ /Ag/g-C ₃ N ₄	In-situ growth and photoreduction	Ag	2,4-DCP (10 mg/L)	1	500 W Xe lamp with a 400 nm cut-off filter	0.91 h ⁻¹ (g-C ₃ N ₄ : 0.175 h ⁻¹)	(Gong et al., 2017)
Ag ₂ CrO ₄ -GO	Precipitation	-	MB (1 × 10 ⁻⁵ mol/L, 100 mL)	0.2	300 W Xe lamp with a 400 nm cut-off filter	0.28 min ⁻¹ (GO: ~0.08 min ⁻¹)	(Xu et al., 2015b)
Ag ₂ CrO ₄ /g-C ₃ N ₄	Precipitation	-	MO (10 mg/L); RhB (10 mg/L)	0.4	300 W Xe lamp (λ > 400 nm)	0.0964 min ⁻¹ for MO; 0.0921 min ⁻¹ for RhB (g-C ₃ N ₄ : 0.0159 min ⁻¹ for MO; 0.0089 min ⁻¹ for RhB)	(Deng et al., 2016)
Ag ₂ CrO ₄ /N-GQDs@g-C ₃ N ₄	Freeze-drying and reflux	N-GQDs	DC (50 mg/L)	0.5	300 W Xe lamp with 420 nm and 760 nm cut-off filter	0.04052 min ⁻¹ under visible; 0.004 min ⁻¹ under near-infrared (g-C ₃ N ₄ : 0.00705 min ⁻¹ under visible)	(Feng et al., 2018)
Ag ₂ CO ₃ /Ag/WO ₃	Deposition and photochemical reduction	Ag	RhB (20 mg/L); MO, CIP and TC (10 mg/L)	0.5	300 W Xe lamp with a 420 nm cut-off filter	0.08613 min ⁻¹ (WO ₃ : 0.0013 min ⁻¹)	(Yuan et al., 2017a)
Ag ₂ CO ₃ /Ag/AgBr	Photoreduction and an ion exchange	Ag	RhB (20 mg/L); MO (20 mg/L)	0.25	500 W Xe lamp with a 420 nm cut-off filter	0.098 min ⁻¹ for RhB; 0.1073 min ⁻¹ for MO (Ag ₂ CO ₃ /Ag: 0.003 min ⁻¹ for RhB; 0.0013 min ⁻¹ for MO)	(Hu et al., 2015)
Ag ₂ CO ₃ /g-C ₃ N ₄	Direct growth	Ag	RhB (5 mg/L)	1	300 W Xe lamp (λ ≥ 400 nm)	0.1355 min ⁻¹ (g-C ₃ N ₄ : 0.0166 min ⁻¹)	(Lei et al., 2015)
Ag ₂ O/RGO/TiO ₂	Chemical precipitation	RGO	TC (10 mg/L)	0.4	350 W mercury lamp; 300 W Xe arc lamp; 300 W infrared lamp	0.0887 min ⁻¹ under UV; 0.0594 min ⁻¹ under visible; 0.0187 min ⁻¹ under NIR (RGO/TiO ₂ : 0.039 min ⁻¹ under UV; 0.005 min ⁻¹ under visible; 0.0017 min ⁻¹ under NIR)	(Hu et al., 2017)
Ag ₂ O@Ag@BiVO ₄	pH-mediated chemical precipitation	Ag	RhB (10 mg/L); MB (20 mg/L)	0.6	300 W Xe lamp (λ > 420 nm)	0.5208 min ⁻¹ for RhB; 0.1008 min ⁻¹ for MB (BiVO ₄ : 0.0106 min ⁻¹ for RhB; 0.0014 min ⁻¹ for MO)	(Yang et al., 2016)

SMX, Sulfamethoxazole; 2,4-DCP, 2,4-dichlorophenol; MB, Methylene Blue; DC, Doxycycline; UV, Ultraviolet light; NIR, Near-infrared; QD, Quantum Dots; NS, Nanosheet; 2,4-DNP, 2,4-Dinitrophenol; BDE-47, 2,2',4,4'-Tetrabrominateddiphenyl ether; SA, Salicylic Acid.

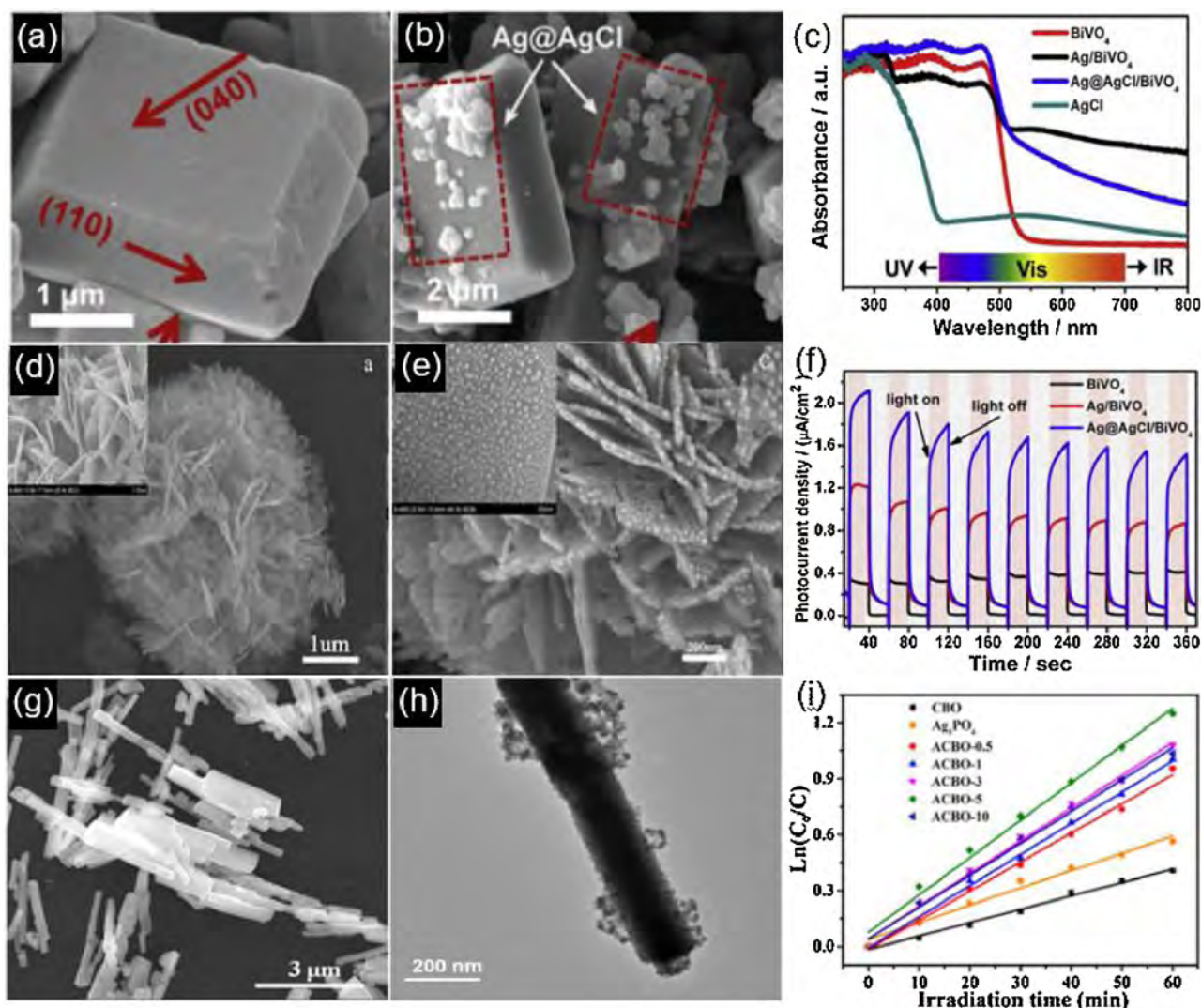


Fig. 7. SEM images of BiVO₄ (a) and Ag@AgCl/BiVO₄ (b); (c) UV-vis diffuse reflectance spectra of the BiVO₄, Ag/BiVO₄, Ag@AgCl/BiVO₄ and AgCl; (f) Transient photocurrent responses of BiVO₄, Ag/BiVO₄, Ag@AgCl/BiVO₄. Reproduced with permission from Ref. Li et al. (2015b). Copyright 2015 Elsevier. SEM images of Bi₂WO₆ (d) and Ag@AgCl/Bi₂WO₆ (e). Reproduced with permission from Ref. Liang et al. (2015). Copyright 2014 Elsevier. (g) SEM image of CuBi₂O₄; (h) TEM image of Ag₃PO₄/CuBi₂O₄ composite; (i) The pseudo-first-order reaction kinetics of the prepared samples for TC degradation. Reproduced with permission from Ref. Shi et al. (2017). Copyright 2014 Elsevier.

properties of other plasmonic metal NPs based Z-scheme photocatalysts were summarized in Table S2. From Table S1 and S2, it could be seen that Ag-based semiconductor photocatalysts had shown superior degradation performance to aqueous solution pollutants. Different from AgCl, AgI or AgBr and other silver-based semiconductors have a relatively narrow bandgaps and can absorb visible light, which can directly form an efficient Z-scheme photocatalytic system with other semiconductor materials. For example, for Ag₃PO₄ ($E_g \sim 2.4$ eV), its {111} facets are the most active crystal facet among all facets owing to the highest surface energy level (Martin et al., 2013). So, it is anticipated to combine two strategies, including hybridization and exposed facets control, to improve the photocatalytic performance of Ag₃PO₄. Tang and co-workers successfully fabricated Ag₃PO₄ {111}/g-C₃N₄ Z-scheme hybrid (Tang et al., 2015). Results showed that the layered g-C₃N₄ was attached on the {111} facets of Ag₃PO₄ via strong interface electrostatic interaction with Ag⁺. The hybrid composite showed the highest photocatalytic performance for MB degradation (0.3214 min^{-1}), which was 8.10 times higher than single g-C₃N₄ (0.0397 min^{-1}). The improved photocatalytic performance of Ag₃PO₄ {111}/g-C₃N₄ photocatalysts was attributed to the common effect of reactive Ag₃PO₄ {111} facets and the efficient separation of

photogenerated carriers via a Z-scheme system consisting of Ag₃PO₄, Ag and g-C₃N₄, in which Ag NPs acted as charge transmission bridge.

Besides, the photocatalytic activity of photocatalysts is also morphology dependent (Hou et al., 2013a; Cai et al., 2017; Yang et al., 2017; Zhang et al., 2020; Feng et al., 2018). It is generally known that the photocatalyst with hierarchically structure is characterized by large surface area and abundant porous structure, which can provide more active sites and great favor charge carriers transfer, respectively. Liang et al. Liang et al. (2015) decorated Ag@AgCl QDs onto flower-like Bi₂WO₆ surface to form Z-scheme Ag@AgCl/Bi₂WO₆ heterostructure through a facile oil-in-water self-assembly strategy (Fig. 7e). Bi₂WO₆ flower-like structure has a larger surface area with many mesopores (Fig. 7d) and can act as the reaction support to disperse Ag@AgCl. In this heterostructure, the Ag@AgCl/Bi₂WO₆ photocatalyst possessed excellent visible light absorption properties owing to the SPR effect of Ag NPs and the light scattering effect of Bi₂WO₆. It was confirmed that the large surface area and tight interface contact of Ag@AgCl/Bi₂WO₆ heterojunction could promote the efficient separation of photo-generated carriers. Similarly, AgCl/Ag/γ-TaON hierarchical hollow spheres (Hou et al., 2013a), AgI/Bi₂WO₆ hierarchical microspheres (Xue et al., 2019b), Ag₃PO₄/In₂S₃ hierarchical microspheres (Yan et al.,

2017), were also constructed and displayed excellent photocatalytic activity for organic pollutants degradation.

Moreover, as mentioned in Section 3.3, the photocatalysts with core@shell structure can improve the photostability of photocorroded material. Ag_2CrO_4 ($E_g \sim 1.8$ eV) displaying superior light absorption and electron conductivity, is considered as a promising candidate, but the photocorrosion of Ag_2CrO_4 also occurs in the photocatalytic reaction. A novel core-shell Z-scheme $\text{Ag}_2\text{CrO}_4/\text{N}$ -doped graphene quantum dots (N-GQDs)@g- C_3N_4 photocatalyst with excellent anti-photocorrosion property was prepared by Feng et al. (Feng et al., 2018). Under visible light irradiation, the photogenerated electrons on the CB of Ag_2CrO_4 (core) could migrate to the VB of g- C_3N_4 (shell) with inhibited photocorrosion on basis of Z-scheme transfer pathway. The presence of N-GQDs could effectively promote this transfer process owing to its good electron transfer ability. Thus, the enhanced photogenerated carriers separation and redox ability of the catalyst could be realized. Also, Yang et al. (Yang et al., 2017) successfully fabricated a plasmonic Z-scheme Ag/AgCl/ Ag_2O photocatalyst by in-situ growth of Ag/AgCl nanoshell on Ag_2O NPs surface. Under visible light irradiation, the Ag/AgCl/ Ag_2O composite showed the optimal photocatalytic activity for ciprofloxacin (CIP) degradation, realizing 91.2 % of degradation efficiency within 100 min. Silver-based Z-scheme photocatalysts other than flower-like and core@shell structure, nanoflakes (Wang et al., 2019; Li et al., 2018), rod-like (Shi et al., 2017; Hu et al., 2015), etc. are also fabricated by researchers. For example, a rod-like Z-scheme $\text{Ag}_3\text{PO}_4/\text{CuBi}_2\text{O}_4$ composite photocatalyst was prepared through an in-situ precipitation route (Fig. 7g and h) (Shi et al., 2017). The Ag_3PO_4 (5 wt. %)/ CuBi_2O_4 photocatalyst possessed the best photocatalytic performance for TC degradation, which was 2.16 and 2.79 times higher than that of CuBi_2O_4 and Ag_3PO_4 , respectively (Fig. 7i). It was demonstrated that a small amount of Ag NPs was generated on Ag_3PO_4 surface in the early stage of photocatalytic reaction. Specially, under visible light, the photogenerated electrons formed on the CB of Ag_3PO_4 could move to Ag NPs, and subsequently combined with the photogenerated holes on the VB of CuBi_2O_4 . Meanwhile, the photogenerated electrons generated on the CB of CuBi_2O_4 could reduce O_2 to form $\cdot\text{O}_2^-$, the photogenerated holes on VB of Ag_3PO_4 could oxidize OH^- to $\cdot\text{OH}$ or directly oxidize organic pollutants. In this system, $\cdot\text{O}_2^-$, $\cdot\text{OH}$, and holes were the main active radicals for TC degradation. In addition, abundant and cheap carbon materials (such as GO and its derivatives) have been also utilized to improve the photocatalytic performance of silver-based semiconductor photocatalysts owing to their unique structure and remarkable properties (Xu et al., 2015b; Hu et al., 2017; Cai et al., 2017; Zhang et al., 2020; Sheydaei et al., 2018). Corresponding examples can be found in the previous Section.

5.1.2.2. Photodegradation of gaseous organic pollutants. Volatile organic compounds are typical harmful air organic pollutants (He et al., 2019). Photocatalytic oxidation, which can mineralize volatile organic compounds under mild reaction conditions using light irradiation (Mamaghani et al., 2017), is an efficient method for its degradation. As a gaseous volatile organic compounds, ethylene (C_2H_4) gas in the atmosphere can induce physiological disorders and disease susceptibility even in a trace amount (Keller et al., 2013; Chen et al., 2017b, 2014). Chen et al. (Chen et al., 2017b) fabricated for the first time a series of In_2O_3 -Ag- Ag_3PO_4 Z-scheme photocatalysts through a facile route and examined their performance on C_2H_4 photodegradation under visible light irradiation. When In_2O_3 -Ag- Ag_3PO_4 composite displayed a mass ratio of 9:1 (90-IO-Ag-10-AP), the highest activity for C_2H_4 photodegradation was obtained, and 200 ppm of C_2H_4 was completely decomposed under visible light within 2 h (Fig. 8a). The photocatalytic oxidation reactions well followed with the kinetics of the pseudo-first-order reaction kinetics (Fig. 8b). And the 90-IO-Ag-10-AP composite exhibited the highest k value of $52.93 \times 10^{-3} \text{ h}^{-1}$, which was about 61.6-fold higher than that of In_2O_3 and 41.1-fold higher than that of Ag_3PO_4 . To track the photocatalytic oxidation processes of C_2H_4 ,

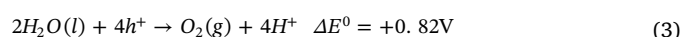
in-situ IR experiment of C_2H_4 photooxidation over the 90-IO-Ag-10-AP composite under visible light illumination was further confirmed (Fig. 8c). According to the in-situ IR experiment results, except for CO_2 and H_2O , no other intermediate product was detected. Based on the band edge positions of In_2O_3 and Ag_3PO_4 in conjunction with $\text{OH}^-/\cdot\text{OH}$ and $\text{O}_2/\cdot\text{O}_2^-$ redox potentials (Fig. 8d), it was deduced that the Z-scheme charge transfer mechanism was the more suitable mode for the composite (Fig. 8e). This work demonstrated that both the activity of C_2H_4 photocatalytic degradation and Ag_3PO_4 photostabilization are considerably improved by making such a Z-scheme composite. Ji et al. (Ji et al., 2019) constructed Z-scheme heterojunction $\text{Ag}_3\text{PO}_4/\text{Ag}/\text{SrTiO}_3$ (AgPO/Ag/STO) for improving visible light response and redox ability (generate $\cdot\text{OH}$ and $\cdot\text{O}_2^-$), and a satisfactory performance of visible-light photocatalytic toluene, xylene, and benzene oxidation was obtained. The conversions of toluene, xylene, and benzene all exceeded 85 % over AgPO/Ag/STO by photothermocatalytic oxidation with visible light irradiation for 4 h at 90 °C. Moreover, Shen et al. (Shen et al., 2018) designed a Z-scheme g- $\text{C}_3\text{N}_4/\text{Ag}/\text{Ag}_3\text{PO}_4$ composite by an in-situ deposition method. The photocatalytic activity of g- $\text{C}_3\text{N}_4/\text{Ag}/\text{Ag}_3\text{PO}_4$ was tested for gaseous isopropanol. After 4 h irradiation, 63 % of isopropanol was oxidized with acetone as main outcome product. This work is expected to provide a promising photocatalyst for environmental purification. Based on the above analysis, it is indicate that silver-based semiconductor Z-scheme photocatalysts are promising candidates for gaseous organic pollutants degradation.

In conclusion, the construction of silver-based semiconductor Z-scheme photocatalytic systems with other suitable bandgap and structure semiconductor can effectively improve the photocatalytic activity and photostability of silver-based semiconductors. Also, silver-based semiconductors usually act as the facilitators for photogenerated carrier separation and visible light harvesting. Particularly, the degradation efficiency of organic pollutants by silver-based semiconductor Z-scheme photocatalysts can be improved by controlling the crystal facet, structure and morphology of the composites. Meanwhile, loading small number of silver-based semiconductors on other in-expensive materials based on the Z-scheme photocatalytic system can also efficiently cut down its use cost. Moreover, unlike aqueous applications, the applications of silver-based semiconductor Z-scheme photocatalytic systems to gaseous organic pollutants purification are rarely found in literature. Considering its unique advantages, more efforts should be done to design and develop silver-based semiconductor Z-scheme photocatalysts for efficient degradation gaseous organic pollutants.

5.2. Photocatalytic production of hydrogen

5.2.1. Reaction mechanisms

Photocatalytic production of H_2 from water splitting using semiconductors, first discovered in the early 1970s (Fujishima and Honda, 1972), has been considered as a promising technology for solving environmental and energy issues. While, water splitting is an uphill reaction with a Gibbs free energy of 237.13 kJ/mol (Eq. (1)), which consists of two half-reactions, including H_2 evolution (Eq. (2)) and O_2 evolution (Eq. (3)).



According to the theoretical calculation, the minimum bandgap (E_g) of a semiconductor should be 1.23 eV to split water molecules into H_2 and O_2 . Nevertheless, not all semiconductors with bandgap larger than 1.23 eV possess the photocatalytic activity for H_2 evolution. Thermodynamically, for photocatalytic H_2 evolution, the CB potential of a semiconductor must be more negative than the reduction potential of H^+/H_2 (-0.41 V vs. NHE at pH = 7). Kinetically, the realization of a

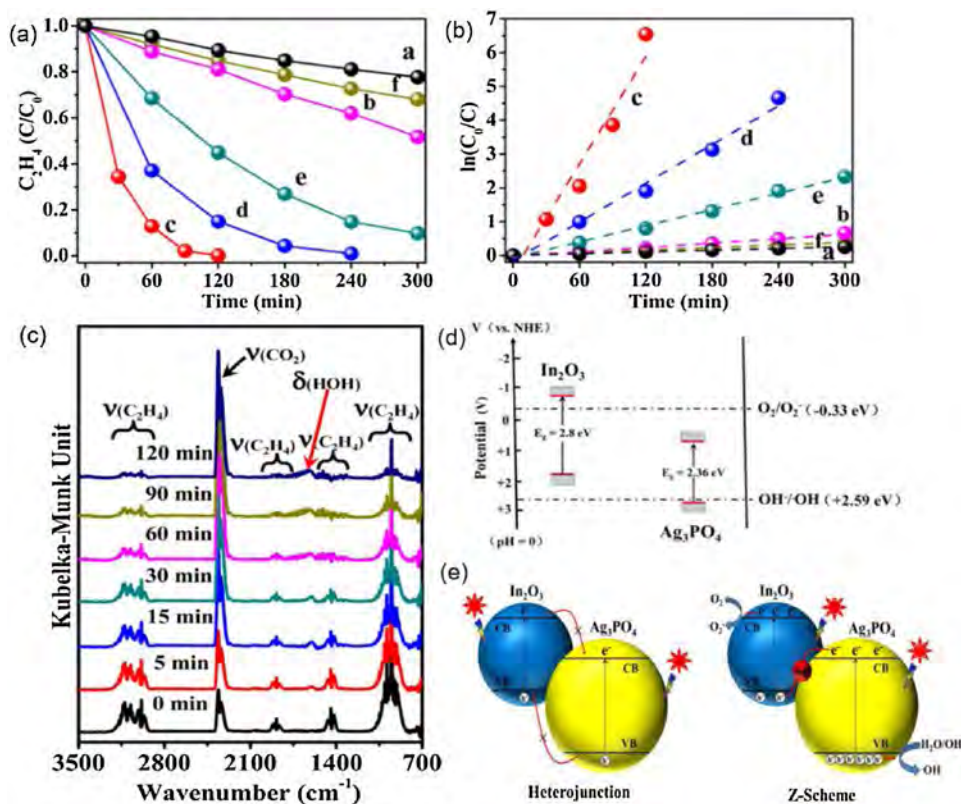


Fig. 8. (a) Time courses of C_2H_4 photo-degradation; (b) pseudo-first-order kinetics plots: a. In_2O_3 , b. 95-I0-Ag-5-AP, c. 90-I0-Ag-10-AP, d. 70-I0-Ag-30-AP, e. 50-I0-Ag-50-AP, f. Ag_3PO_4 ; (c) In-situ IR spectra of ethylene photo-oxidation over 90-I0-Ag-I0-AP composite collected at different illumination times with simulated sunlight; (d) Band edge positions of In_2O_3 and Ag_3PO_4 in conjunction with OH^-/OH and O_2/O_2^- redox potentials; (e) Charge transfer in the conventional $In_2O_3-Ag_3PO_4$ heterojunctions and Z-scheme mode under visible light irradiation. Reproduced with permission from Ref. Chen et al. (2017b). Copyright 2017 Elsevier.

semiconductor photocatalytic production of H_2 still needs four processes as described in the introduction. So, the wide light-absorption range and efficient separation of carriers are two key considerations in developing photocatalysts for H_2 production. Rarely, a semiconductor photocatalyst can meet the mentioned above requirements. Similarly, the same is true for single silver-based semiconductors owing to their relatively positive CB potential and fast recombination of carriers. Fortunately, constructing silver-based semiconductor Z-scheme photocatalytic system seems to be an effective measure for realizing the photocatalytic production of H_2 due to the strong reduction ability, excellent photoabsorption performance, and effective separation of photogenerated carriers (Rauf et al., 2018; Jiang et al., 2018b; Huang et al., 2019c). Moreover, the introduction of suitable sacrificial reagents or co-catalyst can further improve the performance of photocatalysts for photocatalytic production of H_2 . The most common sacrificial reagents are methanol, triethanolamine (TEA), ethanol, and $Na_2S-Na_2SO_3$ solution. These sacrificial agents can react more quickly with photogenerated holes than H_2O because of their less positive oxidation potential, leading to the accumulation of photogenerated electrons on the surface of photocatalysts for the photoreduction of H^+ to H_2 . Pt NPs are commonly used as co-catalyst and active site that can be deposited on a semiconductor surface for H_2 production due to its large work function and superior ability for trapping photogenerated electrons (Ma et al., 2016; Feng et al., 2016). The schematic of photocatalytic production of H_2 of silver-based semiconductor Z-scheme photocatalytic system in the presence of sacrificial agents or co-catalyst is shown in Fig. 9a. In this system, silver-based semiconductor usually located at PS II. The reaction mechanism of photocatalytic H_2 production over silver-based semiconductor Z-scheme photocatalysts is similar to the photocatalytic degradation of pollutants. The difference is that the photogenerated electrons on one semiconductor (PS I) with high CB are shifted to Pt NPs and the electron aggregates, and participate in surface reduction of H^+ . At the same time, the photogenerated holes on other semiconductor (PS II) with low VB could be consumed by sacrificial agents timely, which would favor the separation of photogenerated carriers. For the system

without co-catalyst, the photogenerated electrons on one semiconductor with high CB (PS I) could directly reduce H^+ to form H_2 . In addition, due to the large reaction barrier need to be overcome to produce H_2 by splitting water, therefore, most experiments are carried out in the presence of sacrificial agents.

5.2.2. Application

Photocatalytic production of H_2 is a more challenging process than photodegradation of organic pollutants due to its requirement of large reaction barrier, negative CB potential, and two electrons. So far, researches have shown that silver-based semiconductor Z-scheme photocatalysts can be used for H_2 production from water splitting (Shehzad et al., 2019; You et al., 2018; Che et al., 2018; Zhang et al., 2019a). Recently, Che and co-workers synthesized a Z-scheme $g-C_3N_4/Ag_2CrO_4$ nanocomposite for H_2 evolution with Pt as co-catalyst and methanol as sacrificial agent (Che et al., 2018). Results showed that the single Ag_2CrO_4 exhibited the best photoabsorption performance, suggesting that an effective utilization of solar energy could be obtained over Ag_2CrO_4 . In addition, the introduction of Ag_2CrO_4 significantly enhanced the visible light absorption of the composite. And the higher efficient separation efficiency of photogenerated carriers could be realized in this composite. Especially, the $g-C_3N_4/Ag_2CrO_4$ (23.1 wt.%) nanocomposite displayed the largest H_2 evolution rate of 902.1 $\mu mol/g \cdot h$, which was 14 times higher than $g-C_3N_4$ (Fig. 10a). The enhanced activity was related to the effective separation of photogenerated carriers through the construction of Z-scheme system (Fig. 10c) and the increased light absorption ability due to the photosensitive of Ag_2CrO_4 . Moreover, this nanocomposite was quite stable for H_2 evolution and no significant decrease in activity was detected after 5 cycles (Fig. 10b). Shehzad et al. (Shehzad et al., 2019) fabricated an all-solid-state Z-scheme $AgBr/RGO/TiO_2$ photocatalyst through a facile two-step procedure, in which RGO act as an electron mediator. Methanol was selected as sacrificial agent. The photocatalyst of $AgBr/RGO/TiO_2$ displayed the enhanced photocatalytic H_2 production activity, which was 13.4 times higher than that of single TiO_2 . The enhanced activity was

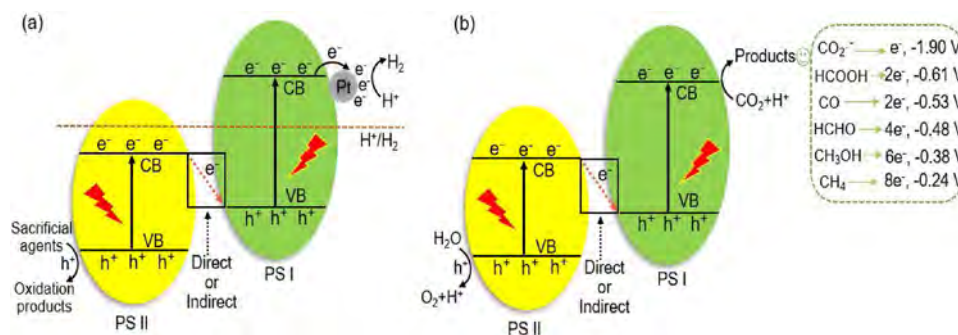


Fig. 9. Schematic illustration of photocatalytic production of H_2 in the presence of sacrificial agents or co-catalyst (a) and photocatalytic reduction of CO_2 (b) of silver-based semiconductor Z-scheme photocatalytic system.

that the efficient transfer of photogenerated carriers and the extended light absorption. Besides, the photocatalysts with large surface area is beneficial to the increase of reactive sites. You et al. You et al. (2018) synthesized a Z-scheme $\text{Ag}_3\text{PO}_4/\text{Ag}/\text{g-C}_3\text{N}_4$ nano-heterojunction by depositing $\text{Ag}_3\text{PO}_4/\text{Ag}$ NPs onto $\text{g-C}_3\text{N}_4$ nanosheets surface. After coupling with $\text{Ag}_3\text{PO}_4/\text{Ag}$ NPs and selecting TEA as sacrificial agent, the composites possessed the improved photocatalytic activity toward H_2 production, which was mainly due to the Z-scheme system of composite and the lamellar structure of the $\text{g-C}_3\text{N}_4$ with large surface area. As listed in Table S2, silver-based semiconductor Z-scheme photocatalysts had better photocatalytic hydrogen production performance than other plasmonic metal NPs based Z-scheme photocatalysts. Moreover, well-defined interfaces and exposed surfaces for Z-scheme photocatalyst are also important factors owing to its advantage to improve the photogenerated carrier separation and light harvesting, which helped to boost its photocatalytic H_2 production performance (Yuan et al., 2017b).

The above results indicate the feasibility of the silver-based semiconductor for H_2 production through construction of Z-scheme photocatalytic system with high CB potential semiconductor. Although the yield of H_2 is low and doesn't meeting the practical application

requires, the potential of silver-based semiconductor Z-scheme photocatalytic systems for producing H_2 cannot be ignored owing to the distinct advantages. In addition, in 2013, An et al. An et al. (2013) had prepared a hollow $\text{AgI}:\text{Ag}$ nanostructures photocatalyst and it exhibited good performance for H_2 production from water reduction. Results showed that the CB potential of AgI in hollow and solid $\text{AgI}:\text{Ag}$ structures was different, and the CB edge of hollow $\text{AgI}:\text{Ag}$ nanostructures (-0.531 eV vs. NHE) was more negative than the reduction potential of H^+/H_2 . It is indicated that engineering the CB position through developing shaped different semiconductor is a feasible method to improve the photocatalytic H_2 production performance of composite. More efforts should be done to explore the shapes of silver-based semiconductor Z-scheme photocatalysts and further enhance their photocatalytic H_2 production performance.

5.3. Photocatalytic reduction of carbon dioxide

5.3.1. Reaction mechanisms

Photocatalytic reduction of CO_2 to renewable fuels can be simultaneously utilized to generate energy and decrease CO_2 content in atmosphere. Generally, the process of photocatalytic CO_2 reduction on

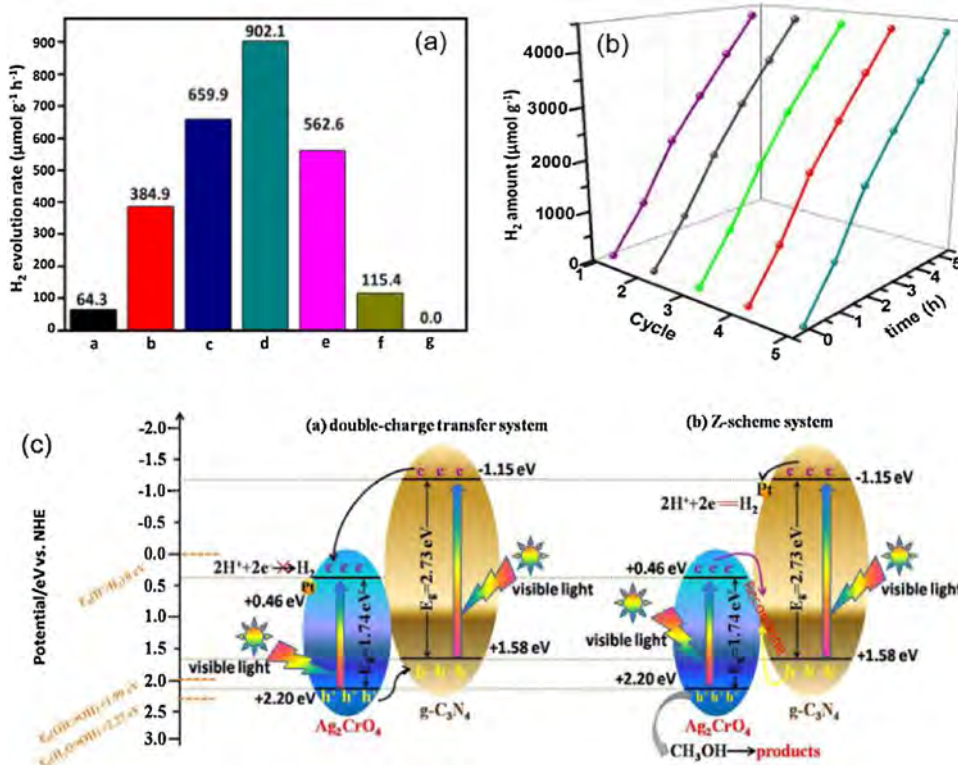


Fig. 10. (a) Comparison of average photocatalytic H_2 production rates; (b) Recyclability of the optimal $\text{g-C}_3\text{N}_4/\text{Ag}_2\text{CrO}_4$ in five successive experiments for the H_2 evolution under visible light irradiation; (c) Schematic representation of the charge generation, migration and H_2 production mechanism of Z-scheme $\text{g-C}_3\text{N}_4/\text{Ag}_2\text{CrO}_4$ nanocomposites. Reproduced with permission from Ref. Che et al. (2018). Copyright 2018 Nature.

Table 3
Thermodynamic potentials of CO₂ reduction into various products.

Equations	Reactions	E ⁰ (V) vs. NHE at pH = 7
1	CO ₂ + e ⁻ → CO ₂ ⁻	-1.90
2	CO ₂ + 2e ⁻ + 2H ⁺ → HCOOH	-0.61
3	CO ₂ + 2e ⁻ + 2H ⁺ → CO + H ₂ O	-0.53
4	CO ₂ + 4e ⁻ + 4H ⁺ → HCHO + H ₂ O	-0.48
5	CO ₂ + 6e ⁻ + 6H ⁺ → CH ₃ OH + H ₂ O	-0.38
6	CO ₂ + 8e ⁻ + 8H ⁺ → CH ₄ + 2H ₂ O	-0.24
7	2H ⁺ + 2e ⁻ → H ₂	-0.41
8	2H ₂ O + 4 h ⁺ → O ₂ + 4H ⁺	+0.82

semiconductor photocatalysts includes five steps: light absorption, carriers separation, adsorption of CO₂, surface redox reaction and products desorption. However, the reduction of CO₂ needs to overcome the big barriers of thermodynamics due to its stable molecular structure (C=O bond energy, 750 kJ/mol) (Kim et al., 2013; Huang et al., 2019d). The redox potentials (E⁰) of different products for CO₂ reduction reactions are obtained from thermodynamic data and presented in Table 3 (Sun et al., 2018; Huang et al., 2019e). Obviously, the process of CO₂ reduction is a proton-combined multiple electron process instead of a one-electron or two-electron transfer. And the reduction reactions of CO₂ are significantly determined by the CB edge of the semiconductor. Moreover, from the point of kinetics, the CO₂ reduction usually require H₂O act as the hydrogen source to form C-H, then, H₂ production from H₂O reduction sometimes may be a key competitive reaction for CO₂ reduction. Therefore, CO₂ reduction reactions are more complex and difficult than H₂ production from water splitting due to the higher thermodynamic stability and kinetic inertness of this process. At present, photocatalytic CO₂ reduction into CH₃OH with H₂O has been reported on Ag/AgCl and Ag/AgBr nanostructures (An et al., 2012). The quantum yields of reduction of CO₂ could obtain 0.893 % and 0.6.9 % with the assistance of Ag/AgCl and Ag/AgBr owing to their strong visible light absorption properties, respectively. But there is still a great need to further boost the activity of photoreduction CO₂ reactions. Considering the excellent advantages of Z-scheme photocatalysts, it is highly expected that constructing silver-based semiconductor Z-scheme photocatalysts is desirable for photocatalytic reduction of CO₂. The schematic of photocatalytic reduction of CO₂ of silver-based semiconductor Z-scheme photocatalytic system is presented in Fig. 9b. Also, silver-based semiconductor usually located at PS II due to the low CB edge. The difference from previous reaction mechanism is that the photogenerated electrons on one semiconductor with high CB (PS I) reacts with CO₂ and H⁺ to produce hydrocarbon fuels. Meanwhile, the photogenerated holes on other semiconductor (PS II) with low VB reacts with H₂O to generate O₂, thereby, accelerating H₂O oxidation can further promote CO₂ reduction.

5.3.2. Application

An all-solid-state Ag₃PO₄/g-C₃N₄ Z-scheme photocatalyst constructed by Fan et al. realized efficient CO₂ photoreduction (He et al., 2015). The addition of Ag₃PO₄ on g-C₃N₄ improved its light absorption properties. Ag NPs, as charge transmission bridge, were generated in the course of photocatalytic reaction. The efficient separation of photogenerated carriers and high redox ability were obtained in this Z-scheme system consisting of Ag₃PO₄, Ag and g-C₃N₄, and then improved the photocatalytic reduction of CO₂ activity of composite. Results revealed that the Ag₃PO₄ (30 wt.)/g-C₃N₄ possessed the highest CO₂ reduction rate of 57.5 μmol/g·h, which was 6.1 times than g-C₃N₄. In another study, Li et al. Li et al. (2015c) loaded AgBr NPs on the surface of g-C₃N₄-decorated nitrogen-doped graphene (ACNNG-x), which presented high photocatalytic performance toward CO₂ reduction. The CO₂ reduction capacity of composite respectively reached 256.45 μmol/g for ethanol and 105.89 μmol/g for methanol (Fig. 11a). Besides, the quantum efficiency of ACNNG-50 was up to 3.41 % at 420

nm, which was 3.5 and 1.7 times higher than single g-C₃N₄ and AgBr, respectively (Fig. 11b). Reasons for this improved photocatalytic activity is due to the Z-scheme carriers transfer mechanism.

Moreover, co-catalysts (usually is noble metal) exert a significant role in the products selectivity and efficiency of photocatalytic CO₂ reduction process (Li et al., 2016b). Noble metal Pt is the most commonly used co-catalyst for CO₂ photoreduction reaction. Interestingly, Xu et al. Xu et al. (2018) using GO as co-catalyst and Ag₂CrO₄ NPs as photosensitizer to fabricate a novel Z-scheme Ag₂CrO₄/g-C₃N₄/GO photocatalyst and found it showed an enhanced CO₂ reduction activity. As presented in Fig. 11c, Ag₂CrO₄ NPs were uniformly dispersed on g-C₃N₄ sheets surface. And an obvious interface between g-C₃N₄ and GO was found, which indicated their compact layered structure is conducive to the rapid transfer of interfacial charges. The density functional theory (DFT) calculations confirmed that Ag₂CrO₄ NPs possessed a smaller effective mass than g-C₃N₄, showing that the transfer of photogenerated electrons from Ag₂CrO₄ to g-C₃N₄ was highly probable (Fig. 11d). Hence, the Z-scheme charge transfer mechanism was formed on the Ag₂CrO₄/g-C₃N₄ composite and the photocorrosion of Ag₂CrO₄ was also inhibited efficiently. Meanwhile, GO, as co-catalyst, not only provide abundant adsorption and catalytic sites, but promote the separation and transport of photogenerated electrons owing to its unique structural characteristics (Fig. 11e). For this system, the enhanced CO₂ reduction activity was attributed to the wider light absorption, high CO₂ adsorption and Z-scheme photocatalytic system. Graphene materials, including GO and RGO, are well known as efficient cocatalysts for g-C₃N₄ due to their superior electron mobility, two-dimensional (2D) layered structure, large surface area and perfect chemical stability. These characteristics make graphene an excellent metal-free cocatalyst alternative to the expensive noble metal Pt. Furthermore, the adsorption of CO₂ is an important step for CO₂ photocatalytic reduction process. As mentioned above, the photocatalyst with high CO₂ adsorption capacity is beneficial to CO₂ reduction. And after the photocatalytic reaction is completed, the final step is product desorption. If the product cannot be released from the catalyst surface timely, the reaction will be terminated and the catalyst will become “poisoned”. In addition, due to the preferential H₂ generation and low CO₂ solubility in solutions, the CO₂ reduction reaction in aqueous solution suffers from low photocatalytic performance (Sato et al., 2011). At present, there are still relatively few applications of photocatalytic reduction of CO₂ based on silver-based semiconductor Z-scheme photocatalytic systems, to which researchers should pay more attention.

6. Powerful combination of silver-based semiconductor with MOFs as a novel Z-scheme photocatalyst

MOFs are newly emerged as a kind of porous crystalline organic-inorganic hybrid materials, which are formed by self-assembly of organic ligands and metal ions/clusters via coordination bonds (Yaghi et al., 2003; Pi et al., 2018). Their unique features including high porosity, large surface areas, and tunable structure endow them with important application in hydrogen storage (Rowell and Yaghi, 2010), separation (Cheng et al., 2019), drug delivery (Sun et al., 2011; Li et al., 2017), sensing (Cui et al., 2014), and heterogeneous catalysis (Liu et al., 2019). Particularly, in MOFs, the alignment of organic ligands and metal ions/clusters has obvious directivity, which can form different framework pore structures, thus showing different adsorption and optical properties. The photoactive MOFs interact with incident light and present semiconducting properties, and it can drive various photoredox reactions (Liu et al., 2019; Silva et al., 2010). At present, some photoactive MOFs materials have been developed as potential candidates for photocatalysis, such as MILs and ZIFs (Liu et al., 2018b; Huang et al., 2018; Xie et al., 2019; Fan et al., 2018; Liu et al., 2017). However, the photocatalytic activity of single MOFs is still unsatisfied due to the rapid recombination of photogenerated carriers and limited light absorption. To further improve its photocatalytic activity, the

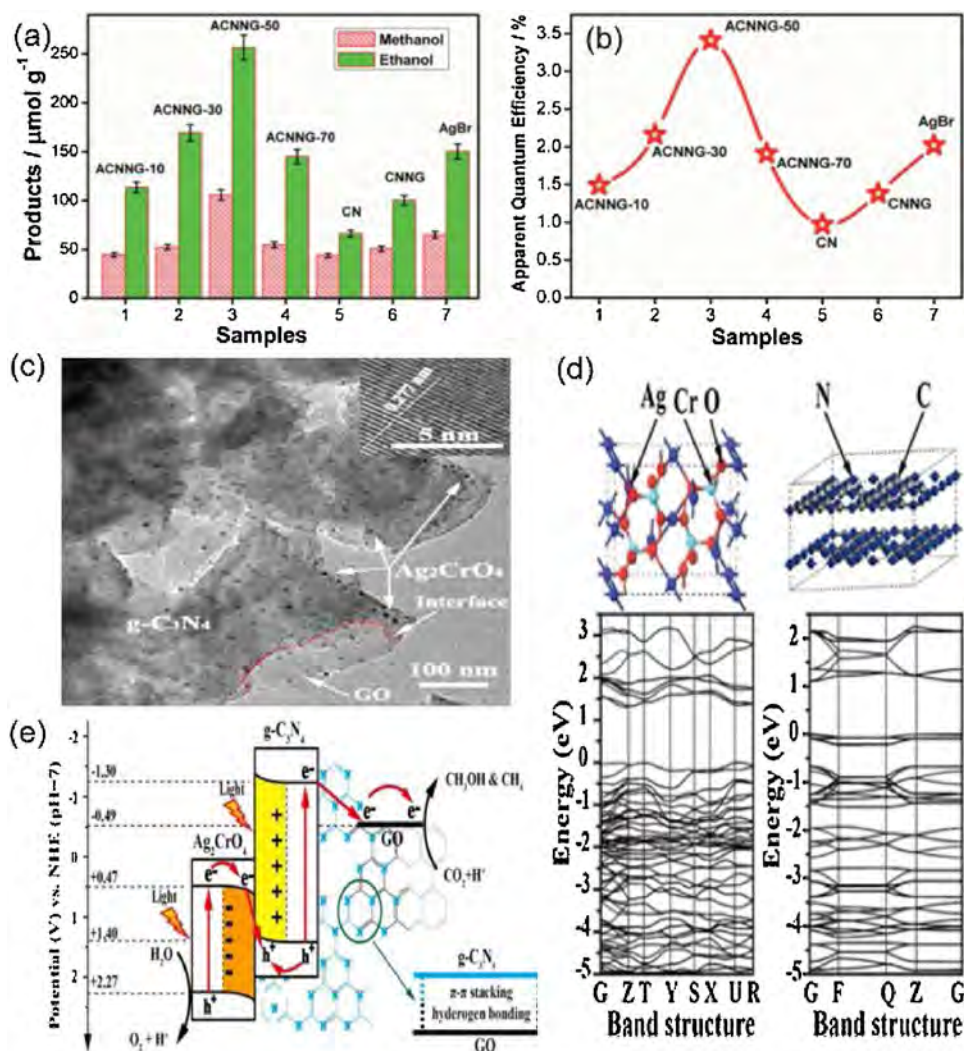


Fig. 11. (a–b) Products of yields from the photocatalytic reduction of CO₂ of different photocatalysts under visible light irradiation and corresponding apparent quantum efficiency for those photocatalysts. Reproduced with permission from Ref. Li et al. (2015c). Copyright 2015 Wiley-VCH. (c) TEM images of Ag₂CrO₄/g-C₃N₄/GO composites and inset of part (c) presents the high-resolution TEM image of Ag₂CrO₄; (d) The crystal and electronic band structures of Ag₂CrO₄ and g-C₃N₄ based on DFT calculation; (e) The proposed Z-scheme photocatalytic mechanism for the Ag₂CrO₄/g-C₃N₄/GO composite. Reproduced with permission from Ref. Xu et al. (2018) Copyright 2018 Elsevier.

combination of light-harvesting catalysts with MOF is proven to be a good strategy. Therefore, considering the excellent photoresponse ability of silver-based semiconductor with the outstanding advantages of Z-scheme photocatalytic system, it is an efficient strategy to construct silver-based semiconductor/MOFs Z-scheme photocatalytic systems (Fan et al., 2018; Liu et al., 2017).

MIL-53(Fe) possessing a suitable optical bandgap ($E_g \sim 2.6$ eV) is considered as an iron-based MOF with photoreactivity because of its flexible structure, semiconductor properties, low cost, and nontoxicity. To further enhance its photocatalytic performance, a plasmonic Z-scheme Ag/AgCl@MIL-53(Fe) photocatalyst was constructed through one-pot solvothermal procedure (Liu et al., 2018b). The photocatalytic activity of Ag/AgCl@MIL-53(Fe) was 21.4 and 10.8 times higher than of single MIL-53(Fe) for RhB degradation and Cr(VI) reduction, respectively. It was depicted in Fig. 12a and b that Ag/AgCl NPs were uniformly anchored on MIL-53(Fe) microrods surface. The HRTEM image of the composite showed that the lattice spacing of 0.24 and 0.28 nm respectively correspond to metallic Ag (111) plane and AgCl (111) plane, demonstrating the successful loading of Ag/AgCl NPs (Fig. 12c–e). The plasmonic Z-scheme photoreaction process was presented in Fig. 12f. Under visible light irradiation, the Ag NPs were SPR-excited to generate electrons and holes, and the plasmon-induced electrons were transferred to the CB of AgCl to reduce Cr(VI), the plasmon-induced holes in Ag were recombine with the photogenerated electron generated in the CB of MIL-53(Fe), the photogenerated holes left on MIL-53(Fe) to oxidize RhB. Then the separation of

photogenerated carriers was realized for improving photocatalytic activity. Moreover, the large surface area and high porosity of MIL-53(Fe) endows Ag/AgCl@MIL-53(Fe) with efficient channel for reactant diffusion, which was also favorable for the photocatalysis. In other similar studies, Huang et al. (2018) designed a plasmonic Z-scheme Ag/AgCl@MIL-88A(Fe) nanocomposites and it exhibited superior performance for ibuprofen degradation under visible light. The introduction of Ag/AgCl promoted the light absorption of MIL-88A(Fe) and greatly accelerated the separation and transfer rate of photo-generated carriers.

Besides, a Z-scheme Ag₃PO₄/MIL-53(Fe) heterojunction photocatalyst fabricated by Xie et al. realized to degrade 93.72 % TC within 60 min under visible light (Xie et al., 2019). The TEM images (Fig. 13a and b) clearly confirmed that Ag₃PO₄ NPs were successfully decorated on MIL-53(Fe) rhombic polyhedron surface. And the APM-3 (Ag₃PO₄:MIL-53(Fe) = 1:3) sample displayed the higher photocatalytic stability than single Ag₃PO₄ after four cyclic experiments (Fig. 13c). XRD analysis indicated that only a weak metallic Ag peak was appeared in the used APM-3 and the peak intensity was much lower than the used Ag₃PO₄ sample, showing the photocorrosion problem of Ag₃PO₄ NPs could be avoided effectively over Ag₃PO₄/MIL-53(Fe) (Fig. 13d). In addition, the composite had the lowest resistance and represented the higher charge transport ability (Fig. 13e). In this study, the Z-scheme mechanism consisting of Ag₃PO₄, Ag, and MIL-53(Fe) was proposed, in which Ag NPs serve as charge transmission bridge (Fig. 13f). Powerful redox ability and effective carriers separation were achieved in this Z-

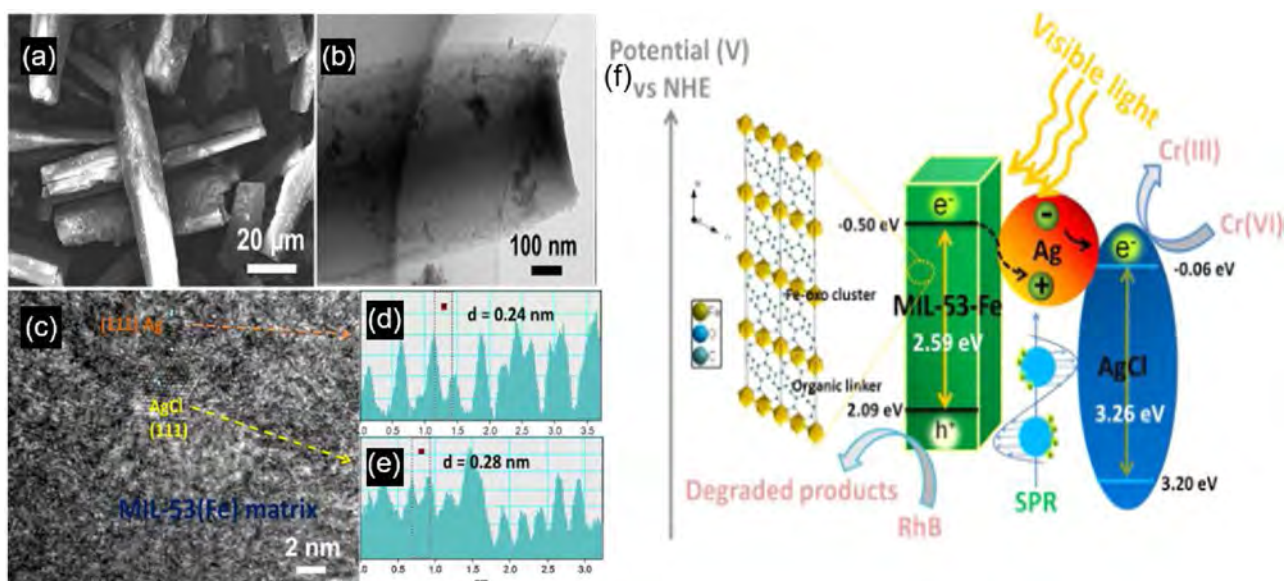


Fig. 12. (a) SEM, (b) TEM, and (c–e) HRTEM image of Ag/AgCl@MIL-53(Fe); (f) Plasmonic Z-scheme photocatalytic mechanism of Ag/AgCl@MIL-53(Fe) under visible light irradiation. Reproduced with permission from Ref. Liu et al. (2018b). Copyright 2017 Elsevier.

scheme heterostructure. Moreover, it is reported that the three-dimensional structure of MOF is beneficial to charge transfer (Zhen et al., 2016). For example, Zhou et al. prepared a novel Z-scheme $\text{Ag}_3\text{PO}_4/\text{MIL-101}/\text{NiFe}_2\text{O}_4$ (APO/MOF/NFO) composite through an in-situ precipitation procedure and the APO/MOF/NFO (20 wt.%) composite displayed excellent photodegradation activity and photostability (Zhou et al., 2018b). It was demonstrated that the improved photocatalytic activity depends on the rapid transfer of photogenerated charge from APO to NFO via the three-dimensional structure of MOF materials (Fig. 14a).

ZIF-8, constructed by Zn^{2+} and imidazolate organic ligands, is

another MOF material that attracts much attention due to its high thermal and chemical stability (Fairen-Jimenez et al., 2011). Fan et al. (2018) synthesized Ag/AgCl@ZIF-8 photocatalyst to degrade acetaminophen (ACT) under visible light (Fig. 14b). Results suggested that Ag/AgCl NPs were uniformly attached to ZIF-8 surface and the presence of ZIF-8 inhibited Ag/AgCl agglomeration to some extent. Due to the wider bandgap, AgCl and ZIF-8 cannot be excited. The SPR effect of Ag NPs was considered as the power supply. Under visible light irradiation, the plasmon-induced electrons of Ag NPs were transferred to the CB of ZIF-8 to reduce O_2 into $\text{O}_2^{\cdot-}$. The improved photocatalytic activity of Ag/AgCl/ZIF-8 was ascribed to the dual roles of ZIF-8, high

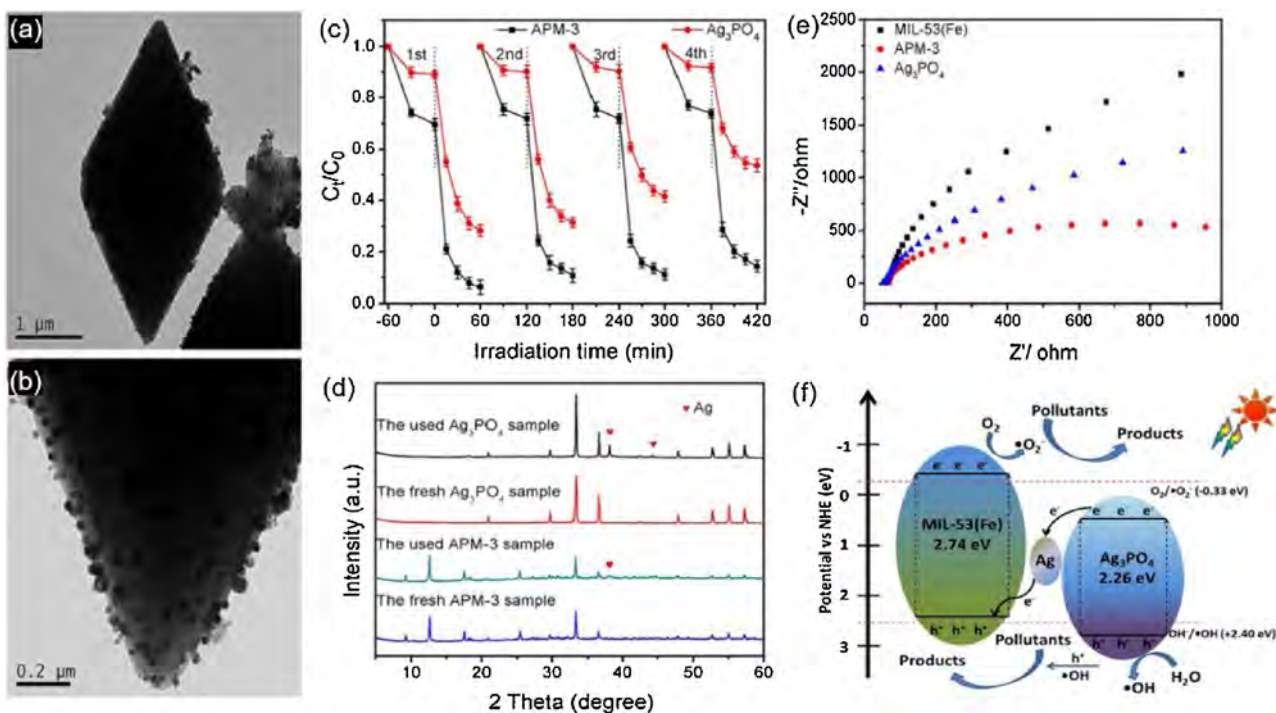


Fig. 13. (a–b) TEM images of APM-3; (c) Cycling photocatalytic tests of Ag_3PO_4 and APM-3 for degradation of TC under visible light irradiation; (d) XRD patterns of the fresh and used Ag_3PO_4 and APM-3; (e) EIS spectra of MIL-53(Fe), Ag_3PO_4 and APM-3; (f) Photocatalytic mechanism scheme and the possible charge separation over APM-3 composite. Reproduced with permission from Ref. Xie et al. (2019). Copyright 2018 Elsevier.

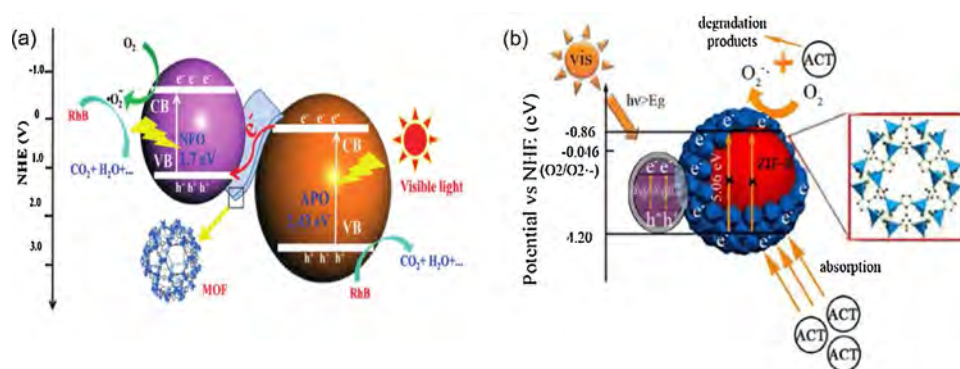


Fig. 14. (a) The photocatalytic mechanism of the APO/MOF/NFO (20 %) composite under visible light irradiation. Reproduced with permission from Ref. Zhou et al. (2018b). Copyright The Royal Society of Chemistry. (b) Proposed photocatalytic mechanism of ACT over the Ag/AgCl@ZIF-8. Reproduced with permission from Ref. Fan et al. (2018). Copyright 2018 Elsevier.

adsorption capacity for pollutants and generation of more O_2^- by the appropriate CB potential. And it was also indicated that when both PS II and PS I cannot be photoexcited, Ag NPs possess SPR effects but the reaction system is not Z-scheme (as discussed in Section 3.2).

In these silver-based semiconductor/MOFs Z-scheme photocatalytic system, MOFs played an important role owing to their large surface area and distinctive structure, and can be summarized as: (i) disperse the silver-based semiconductor; (ii) stabilize and reduce the photocorrosion of silver-based semiconductor; (iii) provide more active sites and increase pollutants adsorption; (iv) promote charge transfer. Also, loading silver-based semiconductor enhances the light absorption ability of MOFs and promotes the separation of photogenerated carriers by a Z-scheme system. Therefore, their combination further improves the performance of photocatalysts.

7. Conclusions

This review has summarized the construction and synthesis methods of silver-based semiconductor Z-scheme photocatalytic systems and discussed the different role of Ag NPs. The role of Ag NPs in silver-based all-solid-state Z-scheme photocatalytic systems mainly includes: Ag SPR effect and charge transmission bridge. While, the function of Ag NPs depends on the optical response characteristics of semiconductors. When PS II or PS I is photoexcited, the SPR effect of Ag NPs plays significant role. When both PS II and PS I are photoexcited, the Ag NPs mainly act as charge transmission bridge. However, when both PS II and PS I cannot be photoexcited, Ag NPs possess SPR effects but the reaction system is not Z-scheme. Subsequently, we summarized the application of silver-based semiconductor Z-scheme photocatalyst in the fields of organic pollutants degradation, photocatalytic H_2 generation, CO_2 reduction, discussing the reaction mechanism and difficult level of these photocatalytic application. It was indicated that integrating silver-based semiconductor with other photocatalyst to construct Z-scheme photocatalytic systems could significantly improve the photocatalytic activity of composite photocatalyst, and enhance the stability and reduce the amount used and costs of silver-based semiconductor. Moreover, crystal facet, morphology, and interface properties played an important effect on the improvement of photocatalytic performance of silver-based semiconductor Z-scheme photocatalytic systems. Finally, the novel combination of silver-based semiconductor with MOFs based on the Z-scheme photocatalytic system was also highlighted.

8. Prospects

Despite silver-based semiconductor Z-scheme photocatalytic system has certain potential in solving environmental and energy issues, there are still some problems which need further efforts.

- i) It is generally known that silver-based semiconductor is unstable under light irradiation and easily reduced to Ag NPs. Appropriate

amount Ag NPs generated by photocorrosion is conducive to the enhancement of photoactivity and photostability of silver-based semiconductor. Extensive aggregation of Ag NPs would reduce the light adsorption and stability of silver-based semiconductors. However, few researchers have studied the exact amount of Ag NPs generated from silver-based semiconductors photocorrosion during synthesis or photocatalysis process. In addition, the size and shape of Ag NPs have a great influence on the photocatalytic activity of composite. Thus, the development of a facile reduction strategy which can be used to control the size, shape and quantity of Ag NPs in the formation process is highly desirable.

- ii) Significant challenges still remain in the development of facile, efficient, and economic methods for preparing high-quality silver-based semiconductor Z-scheme photocatalysts at the large scale for practical applications. Many factors affecting photocatalytic properties of composites, such as size and shape, crystal facet, porosity, and interface properties, need to be further understood, which is critical for design of silver-based semiconductor Z-scheme photocatalytic systems for photocatalysis application. Some researchers have demonstrated that constructing core@shell structure photocatalysts can significantly improve the photostability of silver-based semiconductor core. Besides, it is anticipated to deepen the understanding of the relationship of semiconductor structure and photocatalytic performance when experimental and computational methods are integrated.
- iii) To meet the needs of practical application, more works are done to investigate the silver-based semiconductor Z-scheme photocatalysts, such as the chemical stability of catalyst during use in different pH or temperatures, photocatalytic selectivity for multiple pollutants, etc. Moreover, the environmental risk of these photocatalysts should be carefully evaluated. In particular, the photocatalytic degradation often cannot completely mineralize pollutants, it is necessary to carefully assess the toxicity of intermediate products. In addition, the reported silver-based semiconductor Z-scheme photocatalyst mainly exists in water in the form of solid powder, which is difficult to recover after photocatalytic reaction. Thus, construction of Z-scheme system by coupling of silver-based semiconductor with recyclable magnetic materials is beneficial to reuse and does not cause secondary pollution.
- iv) Although silver-based semiconductor Z-scheme photocatalytic systems with excellent catalytic activities have been fabricated and reported for photocatalytic production of H_2 and reduction of CO_2 , the energy conversion efficiency is far away from industrialization demands and there still exist some challenges in future studies. Generally, photogenerated holes need to be consumed by sacrificial agents timely to obtain high photocatalytic activity for H_2 production, but the addition of sacrificial agent will undoubtedly increase the cost of new energy preparation in the future. The common co-catalyst for H_2 generation is noble metal due to their large work function and the ability for trapping photogenerated electrons. The amount of noble metals deposited on the catalyst surface must be

controlled within a suitable range. Excessive deposition may make the metal become the center of the rapid recombination of electrons and holes, which is not conducive to photocatalytic reaction. In addition, the amount of noble metals on earth is very limited, thus, it is important to develop some cheap and efficient non-noble metal co-catalysts for improving photocatalytic H₂ production. For photocatalytic reduction of CO₂, the selectivity of the products is low due to the CO₂ reduction accompanied by H₂ production and it is a more complicated process (Tu et al., 2014). Co-catalysts modification exerts a significant role in the products selectivity during CO₂ reduction. Moreover, the adsorption of CO₂ and reactant desorption over the photocatalyst surface are two important steps in photocatalytic reduction of CO₂. Combining silver-based semiconductor with large surface area and porosity materials based on the Z-scheme systems is beneficial to the above two steps. Besides, some characterization techniques, such as DFT or scanning tunneling microscopy (STM), can be adopted to better understand the process of CO₂ reduction.

- v) MOFs, as a new type of photocatalyst material, have achieved extensive attention. Emerging research has indicated that silver-based semiconductor/MOFs Z-scheme photocatalytic systems exhibited superior photocatalytic activity for organic pollutants degradation. The advantages of the combination of silver-based semiconductor and MOFs have been discussed in Section 5. However, to date, the reported silver-based semiconductor/MOFs Z-scheme systems are mainly used for the degradation of organic pollutants, more studies should be done on the photocatalytic production of H₂ and reduction of CO₂. Moreover, the development of new types of photoactive MOFs with excellent photocatalytic performance, large surface area, high stability, and well-defined porosity is still urgently needed for the rational design of silver-based semiconductor/MOFs Z-scheme photocatalysts. More morphological structures should be further explored for this system, and not just deposited silver-based semiconductor on the surface of MOFs. We believe that constructing silver-based semiconductor Z-scheme photocatalyst with high photocatalytic activity and photostability is a feasible way for solving environmental and energy issues. We hope this review can provide new insights to researchers for designing silver-based semiconductor Z-scheme photocatalytic systems for solar energy conversion.

Declaration of Competing Interest

The authors declare that they have no known competing financial interests or personal relationships that could have appeared to influence the work reported in this paper.

Acknowledgements

This study was financially supported by Hunan Provincial Innovation Foundation For Postgraduate (CX2018B196), the Program for the National Natural Science Foundation of China (51879101, 51579098, 51779090, 51709101, 51521006, 51809090), the National Program for Support of Top-Notch Young Professionals of China (2014), the Program for Changjiang Scholars and Innovative Research Team in University (IRT-13R17), and Hunan Provincial Science and Technology Plan Project (2018SK20410, 2017SK2243, 2016RS3026), and the Fundamental Research Funds for the Central Universities (531119200086, 531118010114, 531107050978, 541109060031), Shanghai Tongji Gao Tingyao Environmental Science & Technology Development Foundation (STGEF).

Appendix A. Supplementary data

Supplementary material related to this article can be found, in the online version, at doi:<https://doi.org/10.1016/j.jhazmat.2020.122128>.

References

- An, C., Wang, J., Jiang, W., Zhang, M., Ming, X., Wang, S., Zhang, Q., 2012. Strongly visible-light responsive plasmonic shaped AgX: Ag (X = Cl, Br) nanoparticles for reduction of CO₂ to methanol. *Nanoscale* 4, 5646–5650.
- An, C., Wang, J., Liu, J., Wang, S., Sun, Y., 2013. Hollow AgI: Ag nanoframes as solar photocatalysts for hydrogen generation from water reduction. *ChemSuschem* 6, 1931–1937.
- Bai, S., Jiang, J., Zhang, Q., Xiong, Y., 2015. Steering charge kinetics in photocatalysis: intersection of materials syntheses, characterization techniques and theoretical simulations. *Chem. Soc. Rev.* 44, 2893–2939.
- Bing, F., Wu, Z., Liu, J., Zhu, K., Li, Z., Xin, J., Hou, Y., Xi, Q., Cong, M., Liu, P., 2017. Combination of ultrafast dye-sensitized-assisted electron transfer process and novel Z-scheme system: AgBr nanoparticles interspersed MoO₃ nanobelts for enhancing photocatalytic performance of RhB. *Appl. Catal. B: Environ.* 206, 242–251.
- Cai, T., Liu, Y., Wang, L., Zhang, S., Zeng, Y., Yuan, J., Ma, J., Dong, W., Liu, C., Luo, S., 2017. Silver phosphate-based Z-scheme photocatalytic system with superior sunlight photocatalytic activities and anti-photocorrosion performance. *Appl. Catal. B: Environ.* 208, 1–13.
- Cai, T., Liu, Y., Wang, L., Zhang, S., Dong, W., Chen, H., Ma, J., Liu, C., Luo, S., 2019. Ultrafine Ag@AgI nanoparticles on cube single-crystal Ag₃PO₄ (100): an all-day-active Z-scheme photocatalyst for environmental purification. *J. Colloid Interf. Sci.* 533, 95–105.
- Che, Y., Lu, B., Qi, Q., Chang, H., Zhai, J., Wang, K., Liu, Z., 2018. Bio-inspired Z-scheme g-C₃N₄/Ag₂CrO₄ for efficient visible-light photocatalytic hydrogen generation. *Sci. Rep.* 8, 16504.
- Chen, Z., Wang, W., Zhang, Z., Fang, X., 2013. High-efficiency visible-light-driven Ag₃PO₄/AgI photocatalysts: Z-scheme photocatalytic mechanism for their enhanced photocatalytic activity. *J. Phys. Chem. C* 117, 19346–19352.
- Chen, X., Huang, X., Yi, Z., 2014. Enhanced ethylene photodegradation performance of g-C₃N₄-Ag₃PO₄ composites with direct Z-scheme configuration. *Chem. Eur. J.* 20, 17590–17596.
- Chen, F., Yang, Q., Sun, J., Yao, F., Wang, S., Wang, Y., Wang, X., Li, X., Niu, C., Wang, D., Zeng, G., 2016. Enhanced photocatalytic degradation of tetracycline by AgI/BiVO₄ heterojunction under visible-light irradiation: mineralization efficiency and mechanism. *ACS Appl. Mater. Interfaces* 8, 32887–32900.
- Chen, F., Yang, Q., Yao, F., Wang, S., Sun, J., An, H., Yi, K., Wang, Y., Zhou, Y., Wang, L., Li, X., Wang, D., Zeng, G., 2017a. Visible-light photocatalytic degradation of multiple antibiotics by AgI nanoparticle-sensitized Bi₂O₃/I microspheres: enhanced interfacial charge transfer based on Z-scheme heterojunctions. *J. Catal.* 352, 160–170.
- Chen, X., Li, R., Pan, X., Huang, X., Yi, Z., 2017b. Fabrication of In₂O₃-Ag-Ag₃PO₄ composites with Z-scheme configuration for photocatalytic ethylene degradation under visible light irradiation. *Chem. Eng. J.* 320, 644–652.
- Chen, S., Huang, D., Zeng, G., Gong, X., Xue, W., Li, J., Yang, Y., Zhou, C., Li, Z., Yan, X., Li, T., Zhang, Q., 2019. Modifying delafossite silver ferrite with polyaniline: visible-light-response Z-scheme heterojunction with charge transfer driven by internal electric field. *Chem. Eng. J.* 370, 1087–1100.
- Cheng, M., Liu, Y., Huang, D., Lai, C., Zeng, G., Huang, J., Liu, Z., Zhang, C., Zhou, C., Qin, L., Xiong, W., Yi, H., Yang, Y., 2019. Prussian blue analogue derived magnetic Cu-Fe oxide as a recyclable photo-Fenton catalyst for the efficient removal of sulfamethazine at near neutral pH values. *Chem. Eng. J.* 362, 865–876.
- Cui, C., Liu, Y., Xu, H., Li, S., Zhang, W., Cui, P., Huo, F., 2014. Self-assembled metal-organic frameworks crystals for chemical vapor sensing. *Small* 10, 3672–3676.
- Deng, Y., Tang, L., Zeng, G., Wang, J., Zhou, Y., Wang, J., Tang, J., Liu, Y., Peng, B., Chen, F., 2016. Facile fabrication of a direct Z-scheme Ag₂CrO₄/g-C₃N₄ photocatalyst with enhanced visible light photocatalytic activity. *J. Mol. Catal. A-Chem.* 421, 209–221.
- Deng, F., Zhang, Q., Yang, L., Luo, X., Wang, A., Luo, S., Dionysiou, D.D., 2018. Visible-light-responsive graphene-functionalized Bi-bridge Z-scheme black BiOCl/Bi₂O₃ heterojunction with oxygen vacancy and multiple charge transfer channels for efficient photocatalytic degradation of 2-nitrophenol and industrial wastewater treatment. *Appl. Catal. B: Environ.* 238, 61–69.
- Deng, F., Lu, X., Luo, Y., Wang, J., Che, W., Yang, R., Luo, X., Luo, S., Dionysiou, D.D., 2019. Novel visible-light-driven direct Z-scheme CdS/CuInS₂ nanoplates for excellent photocatalytic degradation performance and highly-efficient Cr(VI) reduction. *Chem. Eng. J.* 361, 1451–1461.
- Dong, H., Chen, G., Sun, J., Feng, Y., Li, C., Lv, C., 2014. Stability, durability and regeneration ability of a novel Ag-based photocatalyst, Ag₂Nb₄O₁₁. *Chem. Commun.* 50, 6596–6599.
- Duan, Y., Deng, L., Shi, Z., Zhu, L., Li, G., 2019. Assembly of graphene on Ag₃PO₄/AgI for effective degradation of carbamazepine under visible-light irradiation: mechanism and degradation pathways. *Chem. Eng. J.* 359, 1379–1390.
- Fairen-Jimenez, D., Moggach, S.A., Wharmby, M.T., Wright, P.A., Parsons, S., Düren, T., 2011. Opening the gate: framework flexibility in ZIF-8 explored by experiments and simulations. *J. Am. Chem. Soc.* 133, 8900–8902.
- Fan, G., Zheng, X., Luo, J., Peng, H., Lin, H., Bao, M., Hong, L., Zhou, J., 2018. Rapid synthesis of Ag/AgCl@ZIF-8 as a highly efficient photocatalyst for degradation of acetaminophen under visible light. *Chem. Eng. J.* 351, 782–790.
- Fei, L., Brandl, D.W., Urzhumov, Y.A., Hui, W., Janardan, K., Halas, N.J., Javier, A., Peter, N., 2008. Metallic nanoparticle arrays: a common substrate for both surface-enhanced Raman scattering and surface-enhanced infrared absorption. *ACS Nano* 2, 707–718.
- Feng, J., An, C., Dai, L., Liu, J., Wei, G., Bai, S., Zhang, J., Xiong, Y., 2016. Long-term production of H₂ over Pt/Cds nanoplates under sunlight illumination. *Chem. Eng. J.* 283, 351–357.
- Feng, C., Deng, Y., Tang, L., Zeng, G., Wang, J., Yu, J., Liu, Y., Peng, B., Feng, H., Wang,

- J., 2018. Core-shell $\text{Ag}_2\text{CrO}_4/\text{N-GQDs}@g\text{-C}_3\text{N}_4$ composites with anti-photocorrosion performance for enhanced full-spectrum-light photocatalytic activities. *Appl. Catal. B: Environ.* 239, 525–536.
- Fujishima, A., Honda, K., 1972. Electrochemical photolysis of water at a semiconductor electrode. *Nature* 238, 37–38.
- Gong, Y., Quan, X., Yu, H., Chen, S., 2017. Synthesis of Z-scheme $\text{Ag}_2\text{CrO}_4/\text{Ag}/g\text{-C}_3\text{N}_4$ composite with enhanced visible-light photocatalytic activity for 2, 4-dichlorophenol degradation. *Appl. Catal. B: Environ.* 219, 439–449.
- Gong, X., Huang, D., Liu, Y., Peng, Z., Zeng, G., Xu, P., Cheng, M., Wang, R., Wan, J., 2018. Remediation of contaminated soils by biotechnology with nanomaterials: bio-behavior, applications, and perspectives. *Crit. Rev. Biotechnol.* 38, 455–468.
- Guo, X., Peng, Z., Huang, D., Xu, P., Zeng, G., Zhou, S., Gong, X., Cheng, M., Deng, R., Yi, H., Luo, H., Yan, X., Li, T., 2018a. Biotransformation of cadmium-sulfamethazine combined pollutant in aqueous environments: phanerochaete chrysosporium bring cautious optimism. *Chem. Eng. J.* 347, 74–83.
- Guo, H., Niu, C., Wen, X., Zhang, L., Liang, C., Zhang, X., Guan, D., Tang, N., Zeng, G., 2018b. Construction of highly efficient and stable ternary $\text{AgBr}/\text{Ag}/\text{PbBiO}_3\text{Br}$ Z-scheme photocatalyst under visible light irradiation: performance and mechanism insight. *J. Colloid. Interf. Sci.* 513, 852–865.
- Guo, H., Niu, C., Zhang, L., Wen, X., Liang, C., Zhang, X., Guan, D., Tang, N., Zeng, G., 2018c. Construction of direct Z-Scheme $\text{AgI}/\text{Bi}_2\text{Sn}_2\text{O}_7$ nanojunction system with enhanced photocatalytic activity: accelerated interfacial charge transfer induced efficient Cr(VI) reduction, tetracycline degradation and *Escherichia coli* inactivation. *ACS Sustain. Chem. Eng.* 6, 8003–8018.
- He, Y., Zhang, L., Teng, B., Fan, M., 2015. New application of Z-Scheme $\text{Ag}_3\text{PO}_4/g\text{-C}_3\text{N}_4$ composite in converting CO_2 to fuel. *Environ. Sci. Technol.* 49, 649–656.
- He, J., Cheng, Y., Wang, T., Feng, D., Zheng, L., Shao, D., Wang, W., Wang, W., Lu, F., Dong, H., Zheng, R., Liu, H., 2018. Enhanced photocatalytic performances and magnetic recovery capacity of visible-light-driven Z-scheme $\text{ZnFe}_2\text{O}_4/\text{AgBr}/\text{Ag}$ photocatalyst. *Appl. Surf. Sci.* 440, 99–106.
- He, C., Cheng, J., Zhang, X., Douthwaite, M., Pattison, S., Hao, Z., 2019. Recent advances in the catalytic oxidation of volatile organic compounds: a review based on pollutant sorts and sources. *Chem. Rev.* 119, 4471–4568.
- Hou, J., Yang, C., Wang, Z., Ji, Q., Li, Y., Huang, G., Jiao, S., Zhu, H., 2013a. Three-dimensional Z-scheme $\text{AgCl}/\text{Ag}/\gamma\text{-TaON}$ heterostructural hollow spheres for enhanced visible-light photocatalytic performance. *Appl. Catal. B: Environ.* 142, 579–589.
- Hou, J., Wang, Z., Yang, C., Zhou, W., Jiao, S., Zhu, H., 2013b. Hierarchically plasmonic Z-scheme photocatalyst of Ag/AgCl nanocrystals decorated mesoporous single-crystalline metastable $\text{Bi}_{20}\text{TiO}_{32}$ nanosheets. *J. Phys. Chem. C* 117, 5132–5141.
- Hu, Y., Li, J., Xie, Y., Zhong, Y., 2015. Facile synthesis of Z-scheme $\text{Ag}_2\text{CO}_3/\text{Ag}/\text{AgBr}$ ternary heterostructured nanorods with improved photostability and photoactivity. *J. Mater. Chem. A* 3, 5474–5481.
- Hu, X., Liu, X., Tian, J., Li, Y., Cui, H., 2017. Towards full-spectrum (UV, visible, and near-infrared) photocatalysis: achieving an all-solid-state Z-scheme between Ag_2O and TiO_2 using reduced graphene oxide as the electron mediator. *Catal. Sci. Technol.* 7, 4193–4205.
- Huang, A., Wang, N., Lei, M., Zhu, L., Zhang, Y., Lin, Z., Yin, D., Tang, H., 2013. Efficient oxidative debromination of decabromodiphenyl ether by TiO_2 -mediated photocatalysis in aqueous environment. *Environ. Sci. Technol.* 47, 518–525.
- Huang, D., Hu, C., Zeng, G., Cheng, M., Xu, P., Gong, X., Wang, R., Xue, W., 2017a. Combination of Fenton processes and biotreatment for wastewater treatment and soil remediation. *Sci. Total Environ.* 574, 1599–1610.
- Huang, D., Wang, X., Zhang, C., Zeng, G., Peng, Z., Zhou, J., Cheng, M., Wang, R., Hu, Z., Qin, X., 2017b. Sorptive removal of ionizable antibiotic sulfamethazine from aqueous solution by graphene oxide-coated biochar nanocomposites: influencing factors and mechanism. *Chemosphere* 186, 414–421.
- Huang, W., Jing, C., Zhang, X., Tang, M., Tang, L., Wu, M., Liu, N., 2018. Integration of plasmonic effect into spindle-shaped MIL-88A (Fe): steering charge flow for enhanced visible-light photocatalytic degradation of ibuprofen. *Chem. Eng. J.* 349, 603–612.
- Huang, D., Li, Z., Zeng, G., Zhou, C., Xue, W., Gong, X., Chen, S., Wang, W., Cheng, M., 2019a. Megamerger in photocatalytic field: 2D $g\text{-C}_3\text{N}_4$ nanosheets serve as support of OD nanomaterials for improving photocatalytic performance. *Appl. Catal. B: Environ.* 240, 153–173.
- Huang, D., Li, J., Zeng, G., Xue, W., Chen, S., Li, Z., Deng, R., Yang, Y., Cheng, M., 2019b. Facile construction of hierarchical flower-like Z-scheme $\text{AgBr}/\text{Bi}_2\text{WO}_6$ photocatalysts for effective removal of tetracycline: degradation pathways and mechanism. *Chem. Eng. J.* 375, 121991.
- Huang, D., Liu, C., Zhang, C., Deng, R., Wang, R., Xue, W., Luo, H., Zeng, G., Zhang, Q., Guo, X., 2019c. Cr (VI) removal from aqueous solution using biochar modified with Mg/Al -layered double hydroxide intercalated with ethylenediaminetetraacetic acid. *Bioresour. Technol. Rep.* 276, 127–132.
- Huang, D., Chen, S., Zeng, G., Gong, X., Zhou, C., Cheng, M., Xue, W., Yan, X., Li, J., 2019d. Artificial Z-scheme photocatalytic system: what have been done and where to go? *Coord. Chem. Rev.* 385, 44–80.
- Huang, D., Luo, H., Zhang, C., Zeng, G., Lai, C., Cheng, M., Wang, R., Deng, R., Xue, W., Gong, X., Guo, X., Li, T., 2019e. Nonnegligible role of biomass types and its compositions on the formation of persistent free radicals in biochar: insight into the influences on Fenton-like process. *Chem. Eng. J.* 361, 353–363.
- Ingram, D.B., Linic, S., 2011. Water splitting on composite plasmonic-metal/ semiconductor photoelectrodes: evidence for selective plasmon-induced formation of charge carriers near the semiconductor surface. *J. Am. Chem. Soc.* 133, 5202–5205.
- Ji, W., Rui, Z., Ji, H., 2019. Z-scheme $\text{Ag}_3\text{PO}_4/\text{Ag}/\text{SrTiO}_3$ heterojunction for visible-light induced photothermal synergistic VOCs degradation with enhanced performance. *Ind. Eng. Chem. Res.* 58, 13950–13959.
- Jiang, L., Yuan, X., Zeng, G., Liang, J., Chen, X., Yu, H., Wang, H., Wu, Z., Zhang, J., Xiong, T., 2018a. In-situ synthesis of direct solid-state dual Z-scheme $\text{WO}_3/g\text{-C}_3\text{N}_4/\text{Bi}_2\text{O}_3$ photocatalyst for the degradation of refractory pollutant. *Appl. Catal. B: Environ.* 227, 376–385.
- Jiang, Z., Pan, J., Wang, B., Li, C., 2018b. Two dimensional Z-scheme $\text{AgCl}/\text{Ag}/\text{CaTiO}_3$ nano-heterojunctions for photocatalytic hydrogen production enhancement. *Appl. Surf. Sci.* 436, 519–526.
- Jing, Z., Niu, C., Ji, K., Zhou, L., Zeng, G., 2015. $\text{Ag}/\text{AgCl}/\text{Bi}_2\text{MoO}_6$ composite nanosheets: a plasmonic Z-scheme visible light photocatalyst. *Catal. Commun.* 59, 30–34.
- Kausor, M.A., Gupta, S.S., Chakraborty, D., 2020. Ag_3PO_4 -based nanocomposites and their applications in photodegradation of toxic organic dye contaminated wastewater: review on material design to performance enhancement. *J. Saudi Chem. Soc.* <https://doi.org/10.1016/j.jscs.2019.09.001>.
- Ke, X., Zhang, J., Dai, K., Lv, J., Liang, C., 2019. Novel visible-light-driven direct Z-scheme $\text{Zn}_3\text{V}_2\text{O}_8/\text{Ag}_3\text{PO}_4$ heterojunctions for enhanced photocatalytic performance. *J. Alloys. Compd.* 799, 113–123.
- Keller, N., Ducamp, M.N., Robert, D., Keller, V., 2013. Ethylene removal and fresh product storage: a challenge at the frontiers of chemistry. Toward an approach by photocatalytic oxidation. *Chem. Rev.* 113, 5029–5070.
- Kim, T.W., Kim, I.Y., Jung, T.S., Chang, H.K., Hwang, S.J., 2013. A new type of efficient CO_2 adsorbent with improved thermal stability: self-assembled nanohybrids with optimized microporosity and gas adsorption functions. *Adv. Funct. Mater.* 23, 4377–4385.
- Kim, C.W., Son, Y.S., Kang, M.J., Kim, D.Y., Kang, Y.S., 2016. (040)-crystal facet engineering of BiVO_4 plate photoanodes for solar fuel production. *Adv. Funct. Mater.* 6, 1501754.
- Kothe, T., Plumerg, N., Badura, A., Nowaczyk, M.M., Guschin, D.A., Roegner, M., Schuhmann, W., 2013. Combination of a photosystem 1-based photocathode and a photosystem 2-based photoanode to a Z-scheme mimic for biophotovoltaic applications. *Angew. Chem. Int. Edit.* 52, 14233–14236.
- Kuai, L., Geng, B., Chen, X., Zhao, Y., Luo, Y., 2010. Facile subsequently light-induced route to highly efficient and stable sunlight-driven $\text{Ag}-\text{AgBr}$ plasmonic photocatalyst. *Langmuir* 26, 18723–18727.
- Lei, S., Lin, L., Wang, F., Liu, M., Sun, J., 2015. Enhanced visible-light photocatalytic activity and stability over $g\text{-C}_3\text{N}_4/\text{Ag}_2\text{CO}_3$ composites. *J. Mater. Sci.* 50, 1718–1727.
- Li, C., Zhang, P., Lv, R., Lu, J., Wang, T., Wang, S., Wang, H., Gong, J., 2013. Selective deposition of Ag_3PO_4 on monoclinic BiVO_4 (040) for highly efficient photocatalysis. *Small* 9, 3951–3956.
- Li, G., Wang, Y., Mao, L., 2014. Recent progress in highly efficient Ag-based visible-light photocatalysts. *RSC Adv.* 4, 53649.
- Li, H., Gan, S., Wang, H., Han, D., Niu, L., 2015a. Intercorrelated superhybrid of AgBr supported on graphitic- C_3N_4 -decorated nitrogen-doped graphene: high engineering photocatalytic activities for water purification and CO_2 reduction. *Adv. Mater.* 27, 6906–6913.
- Li, H., Sun, Y., Cai, B., Gan, S., Han, D., Li, N., Wu, T., 2015b. Hierarchically Z-scheme photocatalyst of $\text{Ag}@\text{AgCl}$ decorated on BiVO_4 (040) with enhancing photoelectrochemical and photocatalytic performance. *Appl. Catal. B: Environ.* 170, 206–214.
- Li, H., Gan, S., Wang, H., Han, D., Niu, L., 2015c. Intercorrelated superhybrid of AgBr supported on graphitic- C_3N_4 -decorated nitrogen-doped graphene: high engineering photocatalytic activities for water purification and CO_2 reduction. *Adv. Mater.* 27, 7011–7011.
- Li, H., Tu, W., Zhou, Y., Zou, Z., 2016a. Z-scheme photocatalytic systems for promoting photocatalytic performance: recent progress and future challenges. *Adv. Sci.* 3, 15–25.
- Li, K., Peng, B., Peng, T., 2016b. Recent advances in heterogeneous photocatalytic CO_2 conversion to solar fuels. *ACS Catal.* 7485–7527.
- Li, H., Lv, N., Li, X., Liu, B., Feng, J., Ren, X., Guo, T., Chen, D., Stoddart, J.F., Gref, R., Zhang, J., 2017. Composite CD-MOF nanocrystals-containing microspheres for sustained drug delivery. *Nanoscale* 9, 7454–7463.
- Li, Q.Y., Duan, G.R., Luo, J., Liu, X.H., 2018. Ultrasonic-assisted synthesis of plasmonic Z-scheme $\text{Ag}/\text{AgCl}/\text{WO}_3$ -nanoflakes photocatalyst in geothermal water with enhanced visible-light photocatalytic performance. *J. Energy. Chem.* 27, 826–835.
- Li, H., Deng, F., Zheng, Y., Hua, L., Qu, C., Luo, X., 2019a. Visible-light-driven Z-scheme $\text{rGO}/\text{Bi}_2\text{S}_3\text{-BiOBr}$ heterojunctions with tunable exposed BiOBr (102) facets for efficient synchronous photocatalytic degradation of 2-nitrophenol and Cr(VI) reduction. *Environ. Sci. Nano* 12, 3670–3683.
- Li, X., Xiong, J., Huang, J., Feng, Z., Luo, J., 2019b. Novel $g\text{-C}_3\text{N}_4/h\text{-ZnTiO}_3\text{-a-TiO}_2$ direct Z-scheme heterojunction with significantly enhanced visible-light photocatalytic activity. *J. Alloy Compd.* 774, 768–778.
- Li, X., Xu, P., Chen, M., Zeng, G., Wang, D., Chen, F., Tang, W., Chen, C., Zhang, C., Tan, X., 2019c. Application of silver phosphate-based photocatalysts: barriers and solutions. *Chem. Eng. J.* 366, 339–357.
- Liang, Y., Lin, S., Li, L., Hu, J., Cui, W., 2015. Oil-in-water self-assembled $\text{Ag}@\text{AgCl}$ QDs sensitized Bi_2WO_6 : enhanced photocatalytic degradation under visible light irradiation. *Appl. Catal. B: Environ.* 164, 192–203.
- Liang, C., Zhang, L., Guo, H., Niu, C., Wen, X., Tang, N., Liu, H., Yang, Y., Shao, B., Zeng, G., 2019. Photo-removal of 2, 2', 4, 4'-tetrabromodiphenyl ether in liquid medium by reduced graphene oxide bridged artificial Z-scheme system of $\text{Ag}@\text{Ag}_3\text{PO}_4/g\text{-C}_3\text{N}_4$. *Chem. Eng. J.* 361, 373–386.
- Lin, H., Luo, B., Xu, B., Chen, S., 2012. Synthesis of novel Z-scheme $\text{AgI}/\text{Ag}/\text{AgBr}$ composite with enhanced visible light photocatalytic activity. *Catal. Commun.* 21, 91–95.
- Lin, X., Hou, J., Jiang, S., Lin, Z., Wang, M., Che, G., 2015. A Z-scheme visible-light-driven $\text{Ag}/\text{Ag}_3\text{PO}_4/\text{Bi}_2\text{MoO}_6$ photocatalyst: synthesis and enhanced photocatalytic activity. *RSC Adv.* 5, 104815–104821.
- Liu, J., Liu, N.Y., Li, H., Wang, L.P., Wu, X.Q., Huang, H., Liu, Y., Bao, F., Lifshitz, Y., Lee, S.T., 2016. A critical study of the generality of the two step electron pathway for water splitting by application of a $\text{C}_3\text{N}_4/\text{MnO}_2$ photocatalyst. *Nanoscale* 8,

- 11956–11961.
- Liu, J., Rui, L., Wang, Y., Wang, Y., Zhang, X., Fan, C., 2017. The active roles of ZIF-8 on the enhanced visible photocatalytic activity of Ag/AgCl: generation of superoxide radical and adsorption. *J. Alloys Compd.* 693, 543–549.
- Liu, M., Xue, F., Wang, X., Fu, W., Wang, Y., Lu, Y., Li, N., 2018a. Conformal deposition of atomic TiO₂ layer on chalcogenide nanorod with excellent activity and durability towards solar H₂ generation. *Chem. Eng. J.* 341, 335–343.
- Liu, Q., Zeng, C., Ai, L., Hao, Z., Jiang, J., 2018b. Boosting visible light photoreactivity of photoactive metal-organic framework: designed plasmonic Z-scheme Ag/AgCl@ MIL-53-Fe. *Appl. Catal. B: Environ.* 224, 38–45.
- Liu, Y., Liu, Z., Huang, D., Cheng, M., Zeng, G., Lai, C., Zhang, C., Zhou, C., Wang, W., Jiang, D., Wang, H., Shao, B., 2019. Metal or metal-containing nanoparticle@MOF nanocomposites as a promising type of photocatalyst. *Coord. Chem. Rev.* 388, 63–78.
- Low, J., Yu, J., Jaroniec, M., Wageh, S., Al-Ghamdi, A.A., 2017. Heterojunction photocatalysts. *Adv. Mater.* 29, 1601694.
- Lu, J., Wang, Y., Liu, F., Zhang, L., Chai, S., 2017. Fabrication of a direct Z-scheme type WO₃/Ag₃PO₄ composite photocatalyst with enhanced visible-light photocatalytic performances. *Appl. Surf. Sci.* 393, 180–190.
- Lu, X., Che, W., Hu, X., Wang, Y., Zhang, A., Deng, F., Luo, S., Dionysiou, D.D., 2019. The facile fabrication of novel visible-light-driven Z-scheme CuInS₂/Bi₂WO₆ heterojunction with intimate interface contact by in situ hydrothermal growth strategy for extraordinary photocatalytic performance. *Chem. Eng. J.* 356, 819–829.
- Ma, L., Chen, K., Nan, F., Wang, J., Yang, D., Zhou, L., Wang, Q., 2016. Improved hydrogen production of Au-Pt-Cds hetero-nanostructures by efficient plasmon-induced multipathway electron transfer. *Adv. Funct. Mater.* 26, 6076–6083.
- Maier, S.A., Kik, P.G., Atwater, H.A., Meltzer, S., Harel, E., Koel, B.E., Requicha, A.A.G., 2003. Local detection of electromagnetic energy transport below the diffraction limit in metal nanoparticle plasmon waveguides. *Nat. Mater.* 2, 229–232.
- Mamaghani, A.H., Haghighat, F., Lee, C.S., 2017. Photocatalytic oxidation technology for indoor environment air purification: the state-of-the-art. *Appl. Catal. B: Environ.* 203, 247–269.
- Martin, D.J., Umezawa, N., Chen, X., Ye, J., Tang, J., 2013. Facet engineered Ag₃PO₄ for efficient water photooxidation. *Energ. Environ. Sci.* 6, 3380–3386.
- Meng, S., Ning, X., Zhang, T., Chen, S.F., Fu, X., 2015. What is the transfer mechanism of photogenerated carriers for the nanocomposite photocatalyst Ag₃PO₄/g-C₃N₄, band-band transfer or a direct Z-scheme? *Phys. Chem. Chem. Phys.* 17, 11577–11585.
- Meng, X., Liu, L., Ouyang, S., Xu, H., Wang, D., Zhao, N., Ye, J., 2016. Nanometals for solar-to-chemical energy conversion: from semiconductor-based photocatalysis to plasmon-mediated photocatalysis and photo-thermocatalysis. *Cheminform* 28, 6781–6803.
- Pi, Y., Li, X., Xia, Q., Wu, J., Li, Y., Xiao, J., Li, Z., 2018. Adsorptive and photocatalytic removal of persistent organic pollutants (POPs) in water by metal-organic frameworks (MOFs). *Chem. Eng. J.* 337, 351–371.
- Rauf, A., Ma, M., Kim, S., Msa, S.S., Chung, C.H., Park, J.H., Yoo, P.J., 2018. Mediator- and co-catalyst-free direct Z-scheme composites of Bi₂WO₆-Cu₃P for solar-water splitting. *Nanoscale* 10, 3026–3036.
- Ren, M., Chen, J., Wang, P., Hou, J., Qian, J., Wang, C., Ao, Y., 2018. Construction of silver iodide/silver/bismuth tantalate Z-scheme photocatalyst for effective visible light degradation of organic pollutants. *J. Colloid Interf. Sci.* 532, 190–200.
- Rowell, J.L.C., Yaghi, O.M., 2010. Strategies for hydrogen storage in metal-organic frameworks. *Angew. Chem. Int. Edit.* 44, 4647–4647.
- Sato, S., Arai, T., Morikawa, T., Uemura, K., Suzuki, T.M., Tanaka, H., Kajino, T., 2011. Selective CO₂ conversion to formate conjugated with H₂O oxidation utilizing semiconductor/complex hybrid photocatalysts. *J. Am. Chem. Soc.* 133, 15240–15243.
- Shao, P., Duan, X., Xu, J., Tian, J., Shi, W., Gao, S., Xu, M., Cui, F., Wang, S., 2017. Heterogeneous activation of peroxymonosulfate by amorphous boron for degradation of bisphenol S. *J. Hazard. Mater.* 322, 532–539.
- Shao, B., Liu, Z., Zeng, G., Wu, Z., Liu, Y., Cheng, M., Chen, M., Liu, Y., Zhang, W., Feng, H., 2018a. Nitrogen-doped hollow mesoporous carbon spheres modified g-C₃N₄/Bi₂O₃ direct dual semiconductor photocatalytic system with enhanced antibiotics degradation under visible light. *ACS Sustain. Chem. Eng.* 6, 16424–16436.
- Shao, P., Tian, J., Yang, F., Duan, X., Gao, S., Shi, W., Luo, X., Cui, F., Luo, S., Wang, S., 2018b. Identification and regulation of active sites on nanodiamonds: establishing a highly efficient catalytic system for oxidation of organic contaminants. *Adv. Funct. Mater.* 28, 1705295.
- Shehzad, N., Tahir, M., Johari, K., Murugesan, T., Hussain, M., 2019. Fabrication of highly efficient and stable indirect Z-scheme assembly of AgBr/TiO₂ via graphene as a solid-state electron mediator for visible light induced enhanced photocatalytic H₂ production. *Appl. Surf. Sci.* 463, 445–455.
- Shen, Y., Zhu, Z., Wang, X., Khan, A., Gong, J., Zhang, Y., 2018. Synthesis of Z-scheme g-C₃N₄/Ag/Ag₃PO₄ composite for enhanced photocatalytic degradation of phenol and selective oxidation of gaseous isopropanol. *Mater. Res. Bull.* 107, 407–415.
- Sheydaei, M., Shiadeh, H.R.K., Ayoubi-Feiz, B., Ezziati, R., 2018. Preparation of nano N-TiO₂/graphene oxide/titan grid sheets for visible light assisted photocatalytic ozonation of cefixime. *Chem. Eng. J.* 353, 138–146.
- Shi, W., Song, S., Zhang, H., 2013. Hydrothermal synthetic strategies of inorganic semi-conducting nanostructures. *Chem. Soc. Rev.* 42, 5714–5743.
- Shi, W., Feng, G., Yuan, S., 2017. In situ synthesis of Z-scheme Ag₃PO₄/CuBi₂O₄ photocatalysts and enhanced photocatalytic performance for the degradation of tetracycline under visible light irradiation. *Appl. Catal. B: Environ.* 209, 720–728.
- Silva, C.G., Corma, A., Garcia, H., 2010. Metal-organic frameworks as semiconductors. *J. Mater. Chem.* 20, 3141–3156.
- Song, Z., He, Y., 2017. Novel AgCl/Ag/AgFeO₂ Z-scheme heterostructure photocatalyst with enhanced photocatalytic and stability under visible light. *Appl. Surf. Sci.* 420, 911–918.
- Sorcar, S., Hwang, Y., Grimes, C.A., In, S.I., 2017. Highly enhanced and stable activity of defect-induced titania nanoparticles for solar light-driven CO₂ reduction into CH₄. *Mater. Today.* 20, 507–515.
- Sun, C., Qin, C., Wang, C., Su, Z., Wang, S., Wang, X., Yang, G., Shao, K., Lan, Y., Wang, E., 2011. Chiral nanoporous metal-organic frameworks with high porosity as materials for drug delivery. *Adv. Mater.* 23, 5629–5632.
- Sun, Z., Wang, H., Wu, Z., Wang, L., 2018. g-C₃N₄ based composite photocatalysts for photocatalytic CO₂ reduction. *Catal. Today* 300, 160–172.
- Tan, P., Xi, C., Wu, L., Yan, Y.S., Liu, W., Pan, J., Xiang, X., 2017. Hierarchical flower-like SnSe₂ supported Ag₃PO₄ nanoparticles: towards visible light driven photocatalyst with enhanced performance. *Appl. Catal. B: Environ.* 202, 326–334.
- Tang, C., Liu, E., Fan, J., Hu, X., Ma, Y., Wan, J., 2015. A graphitic-C₃N₄-hybridized Ag₃PO₄ tetrahedron with reactive {111} facets to enhance the visible-light photocatalytic activity. *RSC Adv.* 5, 91979–91987.
- Teng, Z., Xu, Y., Hui, X., Wang, H., Da, Z., Huang, S., Ji, H., Li, H., 2014. In situ oxidation synthesis of visible-light-driven plasmonic photocatalyst Ag/AgCl/g-C₃N₄ and its activity. *Ceram. Int.* 40, 9293–9301.
- Tian, M., Chen, H., Jiang, R., Qian, L., Wang, J., 2012. Plasmon-controlled fluorescence: beyond the intensity enhancement. *J. Phys. Chem. Lett.* 3, 191–202.
- Tu, W., Zhou, Y., Zou, Z., 2014. Photocatalytic conversion of CO₂ into renewable hydrocarbon fuels: state-of-the-art accomplishment, challenges, and prospects. *Adv. Mater.* 26, 4607–4626.
- Wan, J., Xiao, D., Liu, E., Yang, H., Fan, J., Hu, X., 2017. Z-scheme visible-light-driven Ag₃PO₄ nanoparticle@MoS₂ quantum dot/few-layered MoS₂ nanosheet heterostructures with high efficiency and stability for photocatalytic selective oxidation. *J. Catal.* 345, 281–294.
- Wang, P., Huang, B.B., Qin, X.Y., Zhang, X.Y., Dai, Y., Wei, J.Y., Whangbo, M.H., 2008. Ag@AgCl: a highly efficient and stable photocatalyst active under visible light. *Angew. Chem. Int. Edit.* 47, 7931–7933.
- Wang, X., Li, S., Ma, Y., Yu, H., Yu, J., 2011. H₂WO₄·H₂O/Ag/AgCl composite nanoplates: a plasmonic Z-scheme visible-light photocatalyst. *J. Phys. Chem. C* 115, 14648–14655.
- Wang, R., Huang, D., Liu, Y., Peng, Z., Zeng, G., Lai, C., Xu, P., Huang, C., Zhang, C., Gong, X., 2016a. Selective removal of BPA from aqueous solution using molecularly imprinted polymers based on magnetic graphene oxide. *RSC Adv.* 6, 106201–106210.
- Wang, T., Wei, Q., Jiang, D., Chen, L., Di, L., Meng, S., Min, C., 2016b. Synthesis of redox-mediator-free direct Z-scheme AgI/WO₃ nanocomposite photocatalysts for the degradation of tetracycline with enhanced photocatalytic activity. *Chem. Eng. J.* 300, 280–290.
- Wang, X., Yang, J., Ma, S., Zhao, D., Dai, J., Zhang, D., 2016c. In situ fabrication of AgI/AgVO₃ nanoribbon composites with enhanced visible photocatalytic activity for redox reactions. *Catal. Sci. Technol.* 6, 243–253.
- Wang, W., Xu, P., Chen, M., Zeng, G., Zhang, C., Zhou, C., Yang, Y., Huang, D., Lai, C., Cheng, M., Hu, L., Xiong, W., Guo, H., Zhou, M., 2018. Alkali metal assisted synthesis of graphite carbon nitride with tunable band-gap for enhanced visible-light-driven photocatalytic performance. *ACS Sustain. Chem. Eng.* 6, 15503–15516.
- Wang, Z., Chen, M., Huang, D., Zeng, G., Xu, P., Zhou, C., Lai, C., Wang, H., Cheng, M., Wang, W., 2019. Multiply structural optimized strategies for bismuth oxyhalide photocatalysis and their environmental application. *Chem. Eng. J.* 374, 1025–1045.
- Wang, J., Zhang, Q., Deng, F., Luo, X., Dionysiou, D.D., 2020. Rapid toxicity elimination of organic pollutants by the photocatalysis of environment-friendly and magnetically recoverable step-scheme SnFe₂O₄/ZnFe₂O₄ nano-heterojunctions. *Chem. Eng. J.* 379, 122264.
- Wen, X.J., Niu, C.G., Min, R., Zhang, L., Zeng, G.M., 2017. AgI nanoparticles-decorated CeO₂ microspheres photocatalyst for the degradation of organic dye and tetracycline under visible-light irradiation. *J. Colloid Interf. Sci.* 497, 368–377.
- Wen, X.J., Niu, C.G., Guo, H., Zhang, L., Liang, C., Zeng, G.M., 2018a. Photocatalytic degradation of levofloxacin by ternary Ag₂CO₃/CeO₂/AgBr photocatalyst under visible-light irradiation: degradation pathways, mineralization ability, and an accelerated interfacial charge transfer process study. *J. Catal.* 358, 211–223.
- Wen, X.J., Niu, C.G., Zhang, L., Liang, C., Guo, H., Zeng, G.M., 2018b. Photocatalytic degradation of ciprofloxacin by a novel Z-scheme CeO₂-Ag/AgBr photocatalyst: influencing factors, possible degradation pathways, and mechanism insight. *J. Catal.* 358, 141–154.
- Wen, X., Shen, C., Niu, C., Lai, D., Zhu, M., Sun, J., Hu, Y., Fei, Z., 2019. Attachment of Ag/AgCl nanoparticles on CdMoO₄ microspheres for effective degradation of doxycycline under visible light irradiation: degradation pathways and mineralization activity. *J. Mol. Liq.* 288, 111063.
- Wen, X.J., Shen, C.H., Fei, Z.H., Fang, D., Liu, Z.T., Dai, J.T., Niu, C.G., 2020a. Recent developments on AgI based heterojunction photocatalytic systems in photocatalytic application. *Chem. Eng. J.* 383, 123083.
- Wen, X., Lu, Q., Lv, X., Sun, J., Guo, J., Fei, Z., Niu, C., 2020b. Photocatalytic degradation of sulfamethazine using a direct Z-scheme AgI/Bi₄V₂O₁₁ photocatalyst: mineralization activity, degradation pathways and promoted charge separation mechanism. *J. Hazard. Mater.* 385, 121508.
- Xiao, Q., Yu, S., Li, L., Wang, T., Liao, X., Ye, Y., 2017. An overview of advanced reduction processes for bromate removal from drinking water: reducing agents, activation methods, applications and mechanisms. *J. Hazard. Mater.* 324, 230–240.
- Xie, L., Yang, Z., Xiong, W., Zhou, Y., Cao, J., Peng, Y., Li, X., Zhou, C., Xu, R., Zhang, Y., 2019. Construction of MIL-53(Fe) metal-organic framework modified by silver phosphate nanoparticles as a novel Z-scheme photocatalyst: visible-light photocatalytic performance and mechanism investigation. *Appl. Surf. Sci.* 465, 103–115.
- Xu, D.F., Cheng, B., Zhang, J.F., Wang, W.K., Yu, J.G., Ho, W.K., 2015a. Photocatalytic activity of Ag₂MO₄ (M = Cr, Mo, W) photocatalysts. *J. Mater. Chem. A* 3, 20153–20166.
- Xu, D., Bei, C., Cao, S., Yu, J., 2015b. Enhanced photocatalytic activity and stability of Z-

- scheme Ag_2CrO_4 -GO composite photocatalysts for organic pollutant degradation. *Appl. Catal. B: Environ.* 164, 380–388.
- Xu, D., Cheng, B., Wang, W., Jiang, C., Yu, J., 2018. $\text{Ag}_2\text{CrO}_4/\text{g-C}_3\text{N}_4/\text{graphene oxide}$ ternary nanocomposite Z-scheme photocatalyst with enhanced CO_2 reduction activity. *Appl. Catal. B: Environ.* 231, 368–380.
- Xue, W., Peng, Z., Huang, D., Zeng, G., Wan, J., Xu, R., Cheng, M., Zhang, C., Jiang, D., Hu, Z., 2018a. Nanoremediation of cadmium contaminated river sediments: microbial response and organic carbon changes. *J. Hazard. Mater.* 359, 290–299.
- Xue, W., Huang, D., Zeng, G., Wan, J., Zhang, C., Xu, R., Cheng, M., Deng, R., 2018b. Nanoscale zero-valent iron coated with rhamnolipid as an effective stabilizer for immobilization of Cd and Pb in river sediments. *J. Hazard. Mater.* 341, 381–389.
- Xue, W., Huang, D., Li, J., Zeng, G., Deng, R., Yang, Y., Chen, S., Li, Z., Gong, X., Li, B., 2019a. Assembly of AgI nanoparticles and ultrathin $\text{g-C}_3\text{N}_4$ nanosheets codecorated Bi_2WO_6 direct dual Z-scheme photocatalyst: an efficient, sustainable and heterogeneous catalyst with enhanced photocatalytic performance. *Chem. Eng. J.* 373, 1144–1157.
- Xue, W., Peng, Z., Huang, D., Zeng, G., Wen, X., Deng, R., Yang, Y., Yan, X., 2019b. In situ synthesis of visible-light-driven Z-scheme $\text{AgI}/\text{Bi}_2\text{WO}_6$ heterojunction photocatalysts with enhanced photocatalytic activity. *Ceram. Int.* 45, 6340–6349.
- Yaghi, O.M., Michael, O.K., Ockwig, N.W., Chae, H.K., Mohamed, E., Jaheon, K., 2003. Reticular synthesis and the design of new materials. *Nature* 423, 705–714.
- Yan, T., Tian, J., Guan, W., Zheng, Q., Li, W., You, J., Huang, B., 2017. Ultra-low loading of Ag_3PO_4 on hierarchical In_2S_3 microspheres to improve the photocatalytic performance: the cocatalytic effect of Ag and Ag_3PO_4 . *Appl. Catal. B: Environ.* 202, 84–94.
- Yang, Q., Chen, F., Li, X., Wang, D., Zhong, Y., Zeng, G., 2016. Self-assembly Z-scheme heterostructured photocatalyst of $\text{Ag}_2\text{O}/\text{Ag}$ -modified bismuth vanadate for efficient photocatalytic degradation of single and dual organic pollutants under visible light irradiation. *RSC Adv.* 6, 60291–60307.
- Yang, S., Xu, D., Chen, B., Luo, B., Shi, W., 2017. In-situ synthesis of a plasmonic $\text{Ag}/\text{AgCl}/\text{Ag}_2\text{O}$ heterostructures for degradation of ciprofloxacin. *Appl. Catal. B: Environ.* 204, 602–610.
- Yang, Y., Zeng, Z., Zhang, C., Huang, D., Zeng, G., Xiao, R., Lai, C., Zhou, C., Guo, H., Xue, W., Cheng, M., Wang, W., Wang, J., 2018. Construction of iodine vacancy-rich $\text{BiO}/\text{Ag}/\text{AgI}$ Z-scheme heterojunction photocatalysts for visible-light-driven tetracycline degradation: transformation pathways and mechanism insight. *Chem. Eng. J.* 349, 808–821.
- Yang, Q., Ma, Y., Chen, F., Yao, F., Sun, J., Wang, S., Yi, K., Hou, L., Li, X., Wang, D., 2019a. Recent advances in photo-activated sulfate radical-advanced oxidation process (SR-AOP) for refractory organic pollutants removal in water. *Chem. Eng. J.* 378, 122149.
- Yang, Y., Zhang, C., Huang, D., Zeng, G., Huang, J., Lai, C., Zhou, C., Wang, W., Guo, H., Xue, W., Deng, R., Cheng, M., Xiong, W., 2019b. Boron nitride quantum dots decorated ultrathin porous $\text{g-C}_3\text{N}_4$: intensified exciton dissociation and charge transfer for promoting visible-light-driven molecular oxygen activation. *Appl. Catal. B: Environ.* 245, 87–99.
- Ye, L., Liu, J., Gong, C., Tian, L., Peng, T., Ling, Z., 2012. Two different roles of metallic Ag on $\text{Ag}/\text{AgX}/\text{BiOX}$ ($\text{X} = \text{Cl}, \text{Br}$) visible light photocatalysts: surface plasmon resonance and Z-scheme bridge. *ACS Catal.* 2, 1677–1683.
- Ye, C., Wang, X.Z., Li, J.X., Li, Z.J., Li, X.B., Zhang, L.P., Chen, B., Tung, C.H., Wu, L.Z., 2016. Protonated graphitic carbon nitride with surface attached molecule as hole relay for efficient photocatalytic O_2 evolution. *ACS Catal.* 6, 8336–8341.
- Yi, Z., Ye, J., Kikugawa, N., Kako, T., Ouyang, S., Stuart-Williams, H., Yang, H., Cao, J., Luo, W., Li, Z., Liu, Y., Withers, R.L., 2010. An orthophosphate semiconductor with photooxidation properties under visible-light irradiation. *Nat. Mater.* 9, 559–564.
- Yin, Z., Bu, Y., Ren, J., Chen, S., Zhao, D., Zou, Y., Shen, S., Yang, D., 2018. Triggering superior sodium ion adsorption on (2 0 0) facet of mesoporous WO_3 nanosheet arrays for enhanced supercapacitance. *Chem. Eng. J.* 345, 165–173.
- Yin, H., Zhang, M., Yao, J., Luo, Y., Li, P., Liu, X., Chen, S., 2020. Surfactant-assisted synthesis of direct Z-scheme $\text{AgBr}/\beta\text{-Ag}_2\text{WO}_4$ heterostructures with enhanced visible-light-driven photocatalytic activities. *Mater. Sci. Semicon. Proc.* 105, 104688.
- You, M., Pan, J., Chi, C., Wang, B., Zhao, W., Song, C., Zheng, Y., Li, C., 2018. The visible light hydrogen production of the Z-Scheme $\text{Ag}_3\text{PO}_4/\text{Ag}/\text{g-C}_3\text{N}_4$ nanosheets composites. *J. Mater. Sci.* 53, 1978–1986.
- Yu, J., Wang, S., Low, J., Xiao, W., 2013. Enhanced photocatalytic performance of direct Z-scheme $\text{g-C}_3\text{N}_4\text{-TiO}_2$ photocatalysts for the decomposition of formaldehyde in air. *Phys. Chem. Chem. Phys.* 15, 16883–16890.
- Yu, H., Huang, B., Wang, H., Yuan, X., Jiang, L., Wu, Z., Zhang, J., Zeng, G., 2018. Facile construction of novel direct solid-state Z-scheme AgI/BiOBr photocatalysts for highly effective removal of ciprofloxacin under visible light exposure: mineralization efficiency and mechanisms. *J. Colloid Interf. Sci.* 522, 82–94.
- Yuan, X., Jiang, L., Chen, X., Leng, L., Wang, H., Wu, Z., Xiong, T., Liang, J., Zeng, G., 2017a. Highly efficient visible-light-induced photoactivity of Z-scheme $\text{Ag}_2\text{CO}_3/\text{Ag}/\text{WO}_3$ photocatalysts for organic pollutant degradation. *Environ. Sci. Nano* 4, 2175–2185.
- Yuan, Q., Liu, D., Zhang, N., Ye, W., Ju, H., Shi, L., Long, R., Zhu, J., Xiong, Y., 2017b. Noble-metal-free janus-like structures by cation exchange for Z-Scheme photocatalytic water splitting under broadband light irradiation. *Angew. Chem. Int. Edit.* 56, 4206–4210.
- Zhang, Z., Jiang, D., Xing, C., Chen, L., Chen, M., He, M., 2015. Novel AgI -decorated $\beta\text{-Bi}_2\text{O}_3$ nanosheet heterostructured Z-scheme photocatalysts for efficient degradation of organic pollutants with enhanced performance. *Dalton Trans.* 44, 11582–11591.
- Zhang, Y., Wang, L., Park, S.H., Kong, X., Lan, X., Song, Z., Shi, J., 2019a. Single near-infrared-laser driven Z-scheme photocatalytic H_2 evolution on upconversion material@ Ag_3PO_4 @black phosphorus. *Chem. Eng. J.* 375, 121967.
- Zhang, Q., Wang, M., Ao, M., Luo, Y., Zhang, A., Zhao, L., Yan, L., Deng, F., Luo, X., 2019b. Solvothermal synthesis of Z-scheme $\text{AgIn}_5\text{S}_8/\text{Bi}_2\text{WO}_6$ nano-heterojunction with excellent performance for photocatalytic degradation and Cr(VI) reduction. *J. Alloys Compd.* 805, 41–49.
- Zhang, H., Yu, D., Wang, W., Gao, P., Zhang, L., Zhong, S., Liu, B., 2019c. Construction of a novel BON-Br-AgBr heterojunction photocatalysts as a direct Z-scheme system for efficient visible photocatalytic activity. *Appl. Surf. Sci.* 497, 143820.
- Zhang, J., Zhang, Z., Zhu, W., Meng, X., 2020. Boosted photocatalytic degradation of Rhodamine B pollutants with Z-scheme $\text{CdS}/\text{AgBr-rGO}$ nanocomposite. *Appl. Surf. Sci.* 502, 144275.
- Zhen, W., Ma, J., Lu, G., 2016. Small-sized Ni (111) particles in metal-organic frameworks with low over-potential for visible photocatalytic hydrogen generation. *Appl. Catal. B: Environ.* 190, 12–25.
- Zhou, P., Yu, J., Jaroniec, M., 2014. All-solid-state Z-scheme photocatalytic systems. *Adv. Mater.* 26, 4920–4935.
- Zhou, L., Zhang, W., Chen, L., Deng, H., 2017. Z-scheme mechanism of photogenerated carriers for hybrid photocatalyst $\text{Ag}_3\text{PO}_4/\text{g-C}_3\text{N}_4$ in degradation of sulfamethoxazole. *J. Colloid Interface Sci.* 487, 410–417.
- Zhou, C., Lai, C., Xu, P., Zeng, G., Huang, D., Zhang, C., Cheng, M., Hu, L., Wan, J., Liu, Y., Xiong, W., Deng, Y., Wen, M., 2018a. In situ grown $\text{AgI}/\text{Bi}_{12}\text{O}_{17}\text{-Cl}_2$ heterojunction photocatalysts for visible light degradation of sulfamethazine: efficiency, pathway, and mechanism. *ACS Sustain. Chem. Eng.* 6, 4174–4184.
- Zhou, T., Zhang, G., Zhang, H., Yang, H., Ma, P., Li, X., Qiu, X., Liu, G., 2018b. Highly efficient visible-light-driven photocatalytic degradation of rhodamine B by a novel Z-scheme $\text{Ag}_3\text{PO}_4/\text{MIL-101}/\text{NiFe}_2\text{O}_4$ composite. *Catal. Sci. Technol.* 8, 2402–2416.
- Zhu, C., Zhang, L., Jiang, B., Zheng, J., Hu, P., Li, S., Wu, M., Wu, W., 2016a. Fabrication of Z-scheme $\text{Ag}_3\text{PO}_4/\text{MoS}_2$ composites with enhanced photocatalytic activity and stability for organic pollutant degradation. *Appl. Surf. Sci.* 377, 99–108.
- Zhu, J., Liu, S., Yang, Q., Xu, P., Ge, J., Guo, X., 2016b. Fabrication of flower-like $\text{Ag}/\text{AgCl}/\text{Bi}_2\text{WO}_6$ photocatalyst and its mechanism of photocatalytic degradation. *Colloid Surf. A* 489, 275–281.